A Model Investigation of the Role of Air–Sea Interaction in the Climatological Evolution and ENSO-Related Variability of the Summer Monsoon over the South China Sea and Western North Pacific

NGAR-CHEUNG LAU AND MARY JO NATH

NOAA/Geophysical Fluid Dynamics Laboratory, Princeton University, Princeton, New Jersey

(Manuscript received 30 July 2008, in final form 13 January 2009)

ABSTRACT

The summertime northeastward march of the climatological maritime monsoon over the South China Sea (SCS) and subtropical western North Pacific (WNP) is examined using the output from a 200-yr integration of a coupled atmosphere–ocean general circulation model (GCM). Increased cloud cover and surface wind speed during monsoon onset over the SCS in May–June reduce the incoming shortwave flux and enhance the upward latent heat flux at the ocean surface, thereby cooling the local sea surface temperature (SST). The resulting east–west gradient in the SST pattern, with lower temperature in the SCS and higher temperature in the WNP, is conducive to eastward migration of the monsoon precipitation over this region. Upon arrival of the precipitation center in the WNP in July–August, the local circulation changes lead to weakening of the mei-yu–baiu rainband near 30°N. The subsequent increases in local shortwave flux and SST impart a northward tendency to the evolution of the WNP monsoon. Many of these model inferences are supported by a parallel analysis of various observational datasets.

The modulation of the above climatological scenario by El Niño–Southern Oscillation (ENSO) events is investigated by diagnosing the output from the coupled GCM and from experiments based on the atmospheric component of this GCM with SST forcings being prescribed separately in the equatorial Pacific, Indian Ocean, and SCS/WNP domains. During the May period after the peak phase of ENSO, the simulated monsoon onset over the SCS occurs later (earlier) than normal in El Niño (La Niña) events. These changes are primarily remote responses to the anomalous SST forcing in the equatorial Pacific and Indian Ocean. The ENSO-related changes in the SCS/WNP are associated with above-normal (below normal) mei-yu–baiu activity during warm (cold) events. In the ensuing July period of the warm events, the simulated precipitation response over the SCS to the local warm SST anomaly tends to oppose the remote response to SST forcing in the northern Indian Ocean. In the July period of cold events, the equatorial Pacific SST anomaly retains its strength and moves still farther westward. This forcing cooperates with the cold SST anomaly in the SCS in influencing the precipitation pattern in the SCS/WNP sector.

1. Introduction

In recent years, rapid advances have been made in our understanding of the space–time behavior and underlying physical mechanisms of the Asian monsoon system. Such research efforts, as reviewed in the monographs edited by Chang (2004) and Wang (2006), are facilitated by the enhanced availability of observational, modeling, and theoretical tools. Studies of the climatological aspects as well as variability of the Asian monsoon indicate that this complex system may be viewed as a mosaic of several regional components. For instance, by analyzing the evolution of the summer rainy season in various Asia–Pacific sites, Wang and LinHo (2002, see their Fig. 9) have identified the following three main constituents: the Indian monsoon over the Arabian Sea/Indian subcontinent/Bay of Bengal, the maritime monsoon over the South China Sea (SCS)/Philippine Sea (PS)/subtropical western North Pacific (WNP)[1], and the East Asian monsoon over China/Korea/southern Japan. The phenomena in each of these subregions (such as monsoon onset and subsequent development, fluctuations on intraseasonal and interannual time scales, etc.) exhibit rather unique

Corresponding author address: Dr. Ngar-Cheung Lau, NOAA/Geophysical Fluid Dynamics Laboratory, Princeton University, P.O. Box 308, Princeton, NJ 08542-0308.
E-mail: gabriel.lau@noaa.gov

[1] We shall henceforth use the label WNP to refer to the maritime region within 10°–30°N, 120°–160°E.

DOI: 10.1175/2009JCLI2758.1

characteristics. This geographical dependence bears a strong relationship with the local land–sea configuration and orography.

The thermal contrast between the land surface and surrounding oceans is evidently a key factor in driving the landward march of the summer monsoon rainfall over India and China/Korea/Japan. Such land–sea contrasts are much less prominent in the mostly maritime zone of the SCS and WNP. Nonetheless, the observational findings presented by Wang (1994), Murakami and Matsumoto (1994), Wu and Wang (2001), Wu (2002), and Wang and LinHo (2002) indicate that the monsoon precipitation in that region displays a notable tendency to advance northeastward, with onsets over the SCS, PS, and WNP typically occurring in mid-May, mid-June, and the latter half of July, respectively. Wu (2002) noted that the warmest climatological sea surface temperature in that region also follows a similar southwest-to-northeast path during the May–July period. The climatological evolution of the precipitation field in the SCS/WNP region is hence modulated by the development of the underlying SST conditions and associated thermal gradients, in accord with the hypothesis put forth previously by Murakami and Matsumoto (1994). Wu and Wang (2001) and Wu (2002) further demonstrated that the SST pattern in the SCS/WNP region is in turn influenced by the seasonal march of the local precipitation and atmospheric circulation, which alter the intensity of incoming solar radiation and latent heat flux at the ocean surface. The empirical evidence gathered thus far indicates that two-way air–sea interactions play a substantial role in the spatiotemporal development of the climatological SCS/WNP summer monsoon.

Not only does the atmosphere–ocean coupling in the SCS/WNP sector affect the local monsoon climate, it also has strong implications on the atmospheric environment in the neighboring regions, particularly the East Asian monsoon in the China/Korea/Japan sector. Specifically, the northeastward advance of the SCS/WNP monsoon influences the location and strength of the low-level subtropical anticyclone over the western Pacific (Wu 2002). The latter feature is, in turn, closely related to the meridional movement and intensity of the ''Plum Rain'' (mei-yu–baiu) phenomenon over China and Japan (e.g., Ueda et al. 1995; Ueda and Yasunari 1996; Ding 2004). Hence, strong interactions exist between the SCS/WNP and East Asian monsoon systems.

The evolution of the precipitation and SST fields in the SCS/WNP region in individual summers exhibits considerable departures from the climatological scenario as portrayed in the preceding paragraphs. One of the key factors contributing to this interannual variability is the amplitude and phase of the El Niño–Southern Oscillation (ENSO) in the equatorial Pacific. Diagnosis of the observational records by Wu and Wang (2000) indicates that the onset of monsoon rain over the SCS and subsequent northeastward march of this precipitation center to the WNP are typically delayed by several pentads in the summers following the peak phase of warm ENSO events; whereas the onsets occur earlier than normal in the summers following cold events. These ENSO-related precipitation anomalies are accompanied by spatial displacement and intensity changes of the subtropical ridge over the WNP as well as the meridional structure of the monsoon rain belts over southeastern and central China (Shen and Lau 1995; Chang et al. 2000a,b). The observational evidence presented in these and other studies suggests that atmospheric and oceanic variations in the SCS/WNP serve as a conduit linking ENSO signals in the tropical Pacific to the weather and climate patterns over the populated regions of East Asia.

Wu and Wang (2000) investigated the processes contributing to the relationships between ENSO and the SCS/WNP monsoon by examining the response of an atmospheric general circulation model (GCM) to ENSO-related SST anomalies prescribed in two sites: the equatorial eastern-central Pacific and the SCS/WNP sector, where the oceanic conditions are linked to remote ENSO forcing by an ''atmospheric bridge'' (Klein et al. 1999; Lau and Nath 2003). The model analysis of Wu and Wang (2000) suggests that the circulation and rainfall patterns in the SCS/WNP are affected by the SST variability in both aforementioned regions. More recently, Annamalai et al. (2005), Yang et al. (2007), and Xie et al. (2009) presented observational and model evidence linking ENSO-related SST changes in the Indian Ocean to variability of the SCS/WNP monsoon.

The primary focus of the present study is to further delineate the mechanisms contributing to the climatological seasonal march of the SCS/WNP summer monsoon and the modulation of this normal evolution by ENSO variability. Our effort is built on the foundation laid by the observational and modeling works reviewed in the preceding paragraphs. The principal tool for this investigation is the current generation of GCMs developed at the Geophysical Fluid Dynamics Laboratory. In view of the effects of air–sea interaction on both climatology and interannual variability of the SCS/WNP monsoon, much of our attention is devoted to the inferences drawn from a 200-yr simulation with a fully coupled atmosphere–ocean model. Auxiliary experiments with an atmosphere-only GCM are also conducted and analyzed, with the goal of assessing the relative impacts of remote and in situ SST forcing on the SCS/WNP monsoon. An attempt is also made to compare our model

results with available observations and with findings reported in previous studies on this subject.

The GCM tools employed in this study, as well as the observational datasets used for validating the model results, are described in section 2. The nature of the air–sea coupling associated with the northeastward advance of the simulated and observed SCS/WNP monsoon is analyzed in sections 3 and 4. Findings on the perturbations of onset dates of the SCS/WNP during ENSO episodes and on the concomitant changes in the local atmospheric circulation in various stages of the warm season are presented in section 5. Contributions to these variations due to seasonal development of SST forcings from the eastern-central equatorial Pacific, the Indian Ocean, and SCS/WNP are examined in section 6. The main conclusions of this work are summarized and discussed in section 7.

2. Model specifications and observational datasets

Most of the model results shown here are based on a 200-yr segment from a longer integration of GFDL coupled model version 2.1 (CM2.1)—a global GCM with full atmosphere–ocean interaction. The formulation of this model and essential aspects of the simulated climate system are documented by Delworth et al. (2006). The fidelity of the tropical Pacific climate and various ENSO phenomena appearing in this simulation is evaluated by Wittenberg et al. (2006). The atmospheric component (AM2.1) of this coupled model uses a finite volume dynamical core, written by Lin (2004), with a horizontal resolution of 2° of latitude by 2.5° of longitude and 24 vertical layers. The physical processes incorporated in the atmospheric and land subsystems of the model are modified versions of those described previously by the GFDL Global Atmosphere Model Development Team (2004) and Milly and Shmakin (2002), respectively. The numerics and physical parameterizations used in the oceanic component are based on the fourth generation of the Modular Ocean Model (MOM4), coded by Griffies et al. (2003). This ocean model has a basic horizontal resolution of 1° latitude and longitude and 50 vertical layers. In the zonal band between 30°S and 30°N, the meridional resolution increases progressively toward the equator, where the grid spacing reaches ⅓°. Flux exchanges between the atmosphere, ocean, land, and sea ice components are computed at 2-h intervals. Our model analysis is focused on a multicentury control integration of CM2.1 under constant radiative forcing in 1860 (see Table 1 of Delworth et al. 2006).

The model findings are compared with the following observational datasets:

- Horizontal wind at 10-m height and 850 mb from the 40-yr European Centre for Medium-Range Weather Forecasts (ECMWF) Re-Analysis (ERA-40) for the 1960–2000 period (Uppala et al. 2005).
- Precipitation rate compiled by the Global Precipitation Climatology Project (GPCP) for the 1979–2005 period (Huffman et al. 1997; Adler et al. 2003). Pentadal means are based on version 1 of this dataset and are downloaded from the NOAA National Climatic Data Center Web site. Monthly means are based on version 2 of this dataset and are downloaded from the Web site maintained by the Physical Sciences Division of the NOAA Earth System Research Laboratory.
- Long-term averaged SST for individual calendar days, based on the analyses by Reynolds and Smith (1994) for the 1968–96 period and downloaded from the Web site maintained by the Physical Sciences Division of the NOAA Earth System Research Laboratory.
- Shortwave and longwave radiative fluxes at the ocean surface from the International Satellite Cloud Climatology Project (ISCCP) for the 1984–2004 period (Zhang et al. 2004).
- Latent and sensible heat fluxes at the ocean surface (OAFlux), as analyzed by Yu and Weller (2007) for the 1981–2002 period.

The statistical significance of the anomalies to be presented in sections 4–6 is estimated by subjecting the signals to a two-tailed Student's *t* test. Anomalies at or above the 90% or 95% significance level are indicated using various graphical aids, as explained in the captions for Figs. 6–11.

3. Climatological march of the spatial patterns related to the summer monsoon in SCS/WNP

a. Principal circulation and precipitation features

A broad impression of the essential features associated with the summer monsoon in the SCS/WNP sector may be gained from the climatological charts in Fig. 1, which show the simulated and observed distributions of horizontal wind vector at 10-m height and precipitation for the periods of May–June and July–August. In May–June, a cyclonic low-level circulation prevails over the SCS in the model atmosphere (Fig. 1a). This flow pattern is accompanied by enhanced precipitation in the eastern portion of the SCS. In contrast, much of the PS and subtropical WNP is under the influence of an expansive anticyclonic circulation cell with a prominent dry zone in 15°–30°N, 130°–160°E. Situated to the northwest of this surface anticyclone is an elongated belt of heavy precipitation, which extends northeastward from China to southern Japan. The northward or northeastward flows

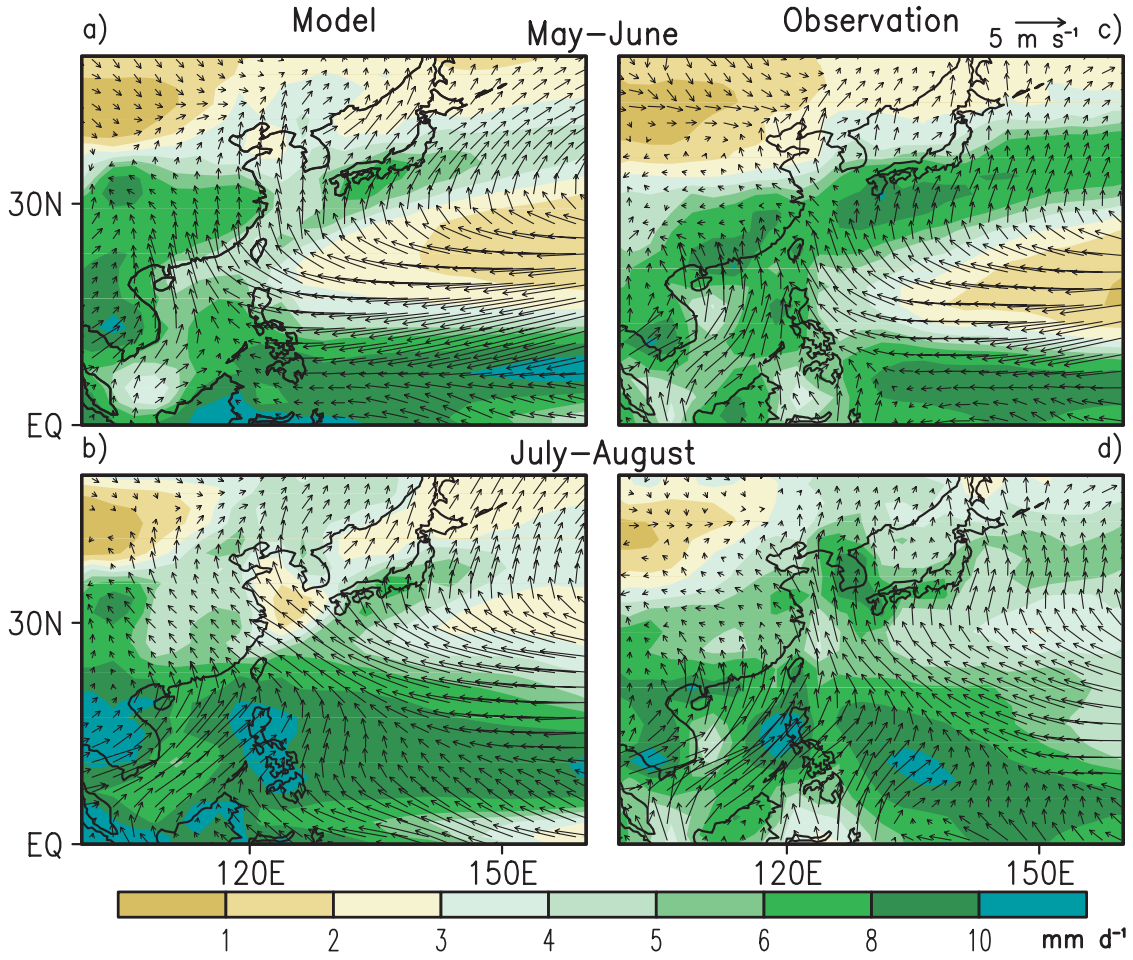

FIG. 1. Climatological distributions of precipitation (shading, see scale bar at bottom) and the surface wind vector [arrows, see scale above (c)] for the (a),(c) May–June and (b),(d) July–August periods. Patterns are based on (left) output from CM2.1 and (right) observational estimates of the GPCP and ERA-40 datasets. In this figure, as well as in Figs. 2–5, the climatological means are computed over the 200-yr output from the CM2.1 integration and over the entire length of record of various observational datasets listed in section 2.

on the southern flank of this rainband serve to transport moisture from the nearby SCS and East China Sea. Most of the above simulated monsoon features are in agreement with those appearing in the observed pattern (Fig. 1c). The observed subtropical rain belt in the China/Japan sector, often referred to by local meteorologists as the ''mei-yu–baiu'' (or Plum Rain) phenomenon (e.g., Ding and Chan 2005), is characterized by higher precipitation rates and a stronger spatial coherence than its model counterpart.

In July–August, the simulated cyclonic flow pattern associated with the monsoon trough over the SCS spreads eastward and covers a large portion of the PS and East China Sea (Fig. 1b). The subtropical ridge over the WNP retreats eastward. The axis of this ridge migrates northward by 5°–10° of latitude. These circulation changes are accompanied by precipitation increases over the Philippines and the WNP within the 10°–20°N belt, northward displacement and reduction in areal extent of the dry zone associated with the subtropical anticyclone over the WNP, and a decrease (increase) in precipitation over central (northeastern) China. The GPCP dataset (Fig. 1d) indicates higher rainfall rates over the WNP near 10°N, 135°W, the East China Sea, and the Korean Peninsula than in the model simulation. As noted by Sperber and Annamalai (2008) and Stowasser et al. (2009), the less intense precipitation east of the Philippines in the model atmosphere (as compared to the observations) may be linked to the excessive strength and westward extent of the equatorial Pacific cold tongue in the simulated SST pattern. The northward advance of the elongated mei-yu–baiu rain belt from early to late summer is more evident in the observed patterns than in the model charts.

b. *Detailed evolution of monsoon features and relationships with surface fluxes*

To highlight the more rapid variations occurring in the course of the seasonal march, consecutive 10-day averages of selected fields are computed, and the changes from one 10-day period to the next are examined. In the left panels of Fig. 2 the distributions of these tendencies in precipitation and 850-mb vector wind, as obtained by subtracting the climatological CM2.1 data for the 10-day period near the end of each calendar month in the warm season from the corresponding data for the succeeding 10-day period, are shown. Inspection of these panels reveals the systematic northeastward movement of a positive precipitation tendency center in the model atmosphere from Indochina in early May (Fig. 2a), to SCS in early June (Fig. 2b), to the PS in early July (Fig. 2c), and to the WNP in early August (Fig. 2d). Cyclonic tendencies of the 850-mb wind prevail to the northwest of the sites of strongest precipitation changes, in accord with the circulation response to tropical heat sources in idealized mechanistic models (e.g., Gill 1980). These cyclonic tendencies are accompanied by easterly or northeasterly wind changes near 30°N, 120°–150°E in Fig. 2c and over central China and the Yellow Sea in Fig. 2d. The circulation changes in these regions impede the prevalent northeastward transport of moisture from the SCS and East China Sea in early summer (see Fig. 1a), and are hence coincident with negative precipitation tendencies (see shading in Figs. 2c,d).

The implications of the circulation and precipitation changes on the fluxes at the ocean surface are studied by plotting the tendencies of simulated downward shortwave (SW) radiative flux (middle column of Fig. 2) and upward latent heat (LH) flux (right column) for the same set of 10-day averages used in constructing the left column. The sign convention adopted here is such that positive tendencies in SW (LH) flux would lead to oceanic warming (cooling). Analogous computations based on model data for longwave radiative flux and sensible heat flux (not shown) yield much weaker tendencies compared to those associated with the SW and LH fluxes.

A strong spatial correspondence exists between the shaded patterns in the left and middle columns of Fig. 2, with positive precipitation tendency being associated with reduced downward SW flux and vice versa. This relationship is attributable to the impact of precipitation changes on the local cloud cover, which in turn modulates the intensity of solar radiation arriving at the ocean surface. Within the tropical and subtropical zones, the distribution of the LH flux tendency (right column of Fig. 2) is linked to changes in the local surface wind speed and sea-to-air humidity gradients through the parameterization scheme for surface fluxes (Beljaars 1995). Increased wind speeds, as would occur when the wind tendency vector (left column of Fig. 2) has a similar orientation as the local climatological wind vector (left column of Fig. 1), lead to enhanced upward transfer of LH. Conversely, opposition of the wind tendency to the mean flow results in a reduction of wind speed and LH flux.

During the May–June period, the arrival of monsoon rainfall at the SCS (Figs. 2a,b) is accompanied by enhanced cloud cover and decreased SW flux (Figs. 2e,f). As a consequence of the strengthening of the southwesterly flow over this region (Figs. 2a,b), the heat loss from the SCS to the atmosphere through LH transfer increases (Figs. 2i,j). These tendencies in both SW and LH fluxes are conducive to cooling of the ocean surface in the SCS. In contrast, the relatively weak precipitation tendencies over the 20°–30°N belt in the WNP during May–June are coincident with positive tendencies in SW flux and surface warming. In early May, the reduced LH flux over much of the subtropical WNP (Fig. 2i) also contributes to warming tendencies of the local waters.

As the center of the positive precipitation tendency continues to migrate toward the PS and WNP in July–August (Figs. 2c,d), the amount of SW radiation arriving at the latter maritime regions is reduced (note negative tendencies in Figs. 2g,h). As noted earlier, a zonally oriented belt of easterly wind tendency and reduced precipitation is seen to develop farther north of the wet zone, thus leading to increased SW flux within 25°–40°N. The SST cooling resulting from the reduced SW flux in the 10°–20°N belt is partially offset by the oceanic warming due to reduced LH loss at the same sites (Figs. 2k,l). Analogously, the warming effects of the increased SW flux in the 25°–40°N zone in Figs. 2g,h are opposed by cooling tendencies due to LH flux changes in the same regions.

In summary, the model results in Fig. 2 are consistent with the observational findings presented by Wu (2002) on the role of air–sea coupling in the climatological evolution of the summer monsoon within the SCS/PS/WNP domain, as portrayed in the schematic diagram and flowchart in his Figs. 11 and 12. The increasing intensity of precipitation and monsoon flow over the SCS during May–June leads to local SST cooling through modulation of SW and LH fluxes; whereas oceanic warming proceeds in several parts of the PS, East China Sea, and WNP during the same period. Under the influence of the resultant east–west gradient of SST changes, the precipitation center migrates eastward toward the relatively warmer waters. A north–south oriented dipole pattern in the vector wind tendency and precipitation fields is then established in the East Asia/WNP sector. The changes in SW and LH fluxes associated with this

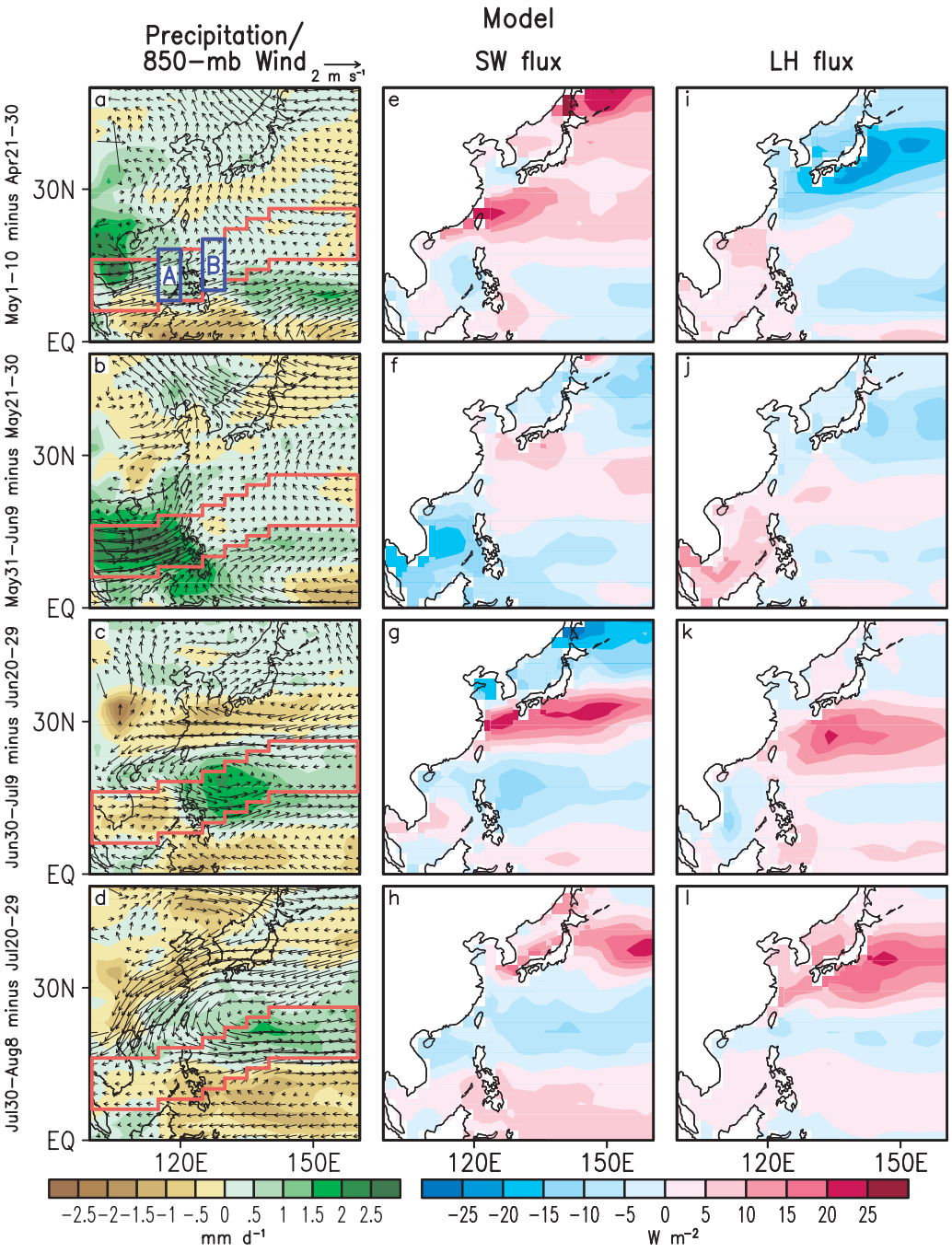

FIG. 2. Distributions of differences between consecutive 10-day means computed by subtracting climatological data for (first row) 21–30 Apr from 1–10 May, (second row) 21–30 May from 31 May–9 Jun, (third row) 20–29 Jun from 30 Jun–9 Jul, and (fourth row) 20–29 Jul from 30 Jul–8 Aug. Tendency charts are shown for (left column) precipitation (shading) and 850-mb wind vector [arrows, see scale above (a)], (middle column) downward shortwave flux, and (right column) upward latent heat flux. Scale bars for precipitation and shortwave/latent heat fluxes are shown in the bottom left and right, respectively. All patterns are based on output from CM2.1. Red line segments in the left panels depict the southwest-to-northeast track of the precipitation signal. In Fig. 4, development along this track is illustrated by taking averages over the 10° lat zone defined by the red line segments for individual longitudes. The blue boxes in (a) correspond to the boundaries of sites A and B used for computing the areal averages shown in Fig. 6.

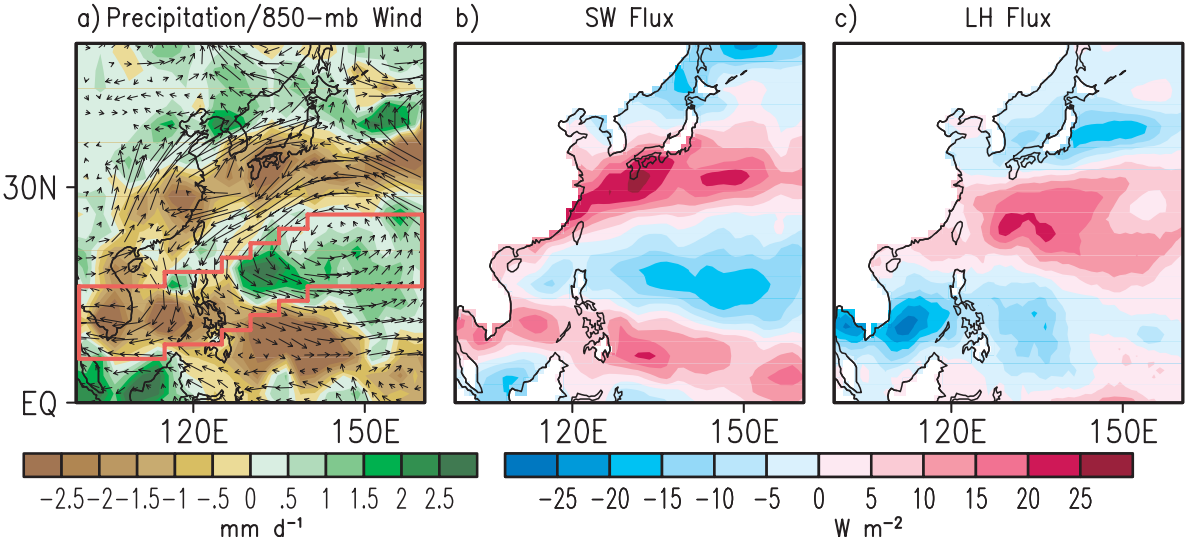

FIG. 3. As in Fig. 2 but for tendencies from 20–29 Jun to 30 Jun–9 Jul based on various observational datasets.

development yield meridional contrasts in SST tendencies, with oceanic cooling near the precipitating zone and warming farther north. This configuration of SST changes imparts a northward component to the movement of the precipitation center over WNP. The seasonal march of the SST field as implied in the above discussion is verified by the sequence of SST tendency charts plotted in the same format as those presented in Fig. 2. These SST patterns (not shown) are characterized by sustained cooling in the SCS during the period from early June to mid-July and continuous northward displacement of the maximum in warming tendencies in the WNP sector throughout the boreal summer.

The model results in Fig. 2 may be evaluated using observational patterns based on the datasets listed in section 2. The tendency from 20–29 June to 30 June–9 July is shown in Fig. 3a for observed precipitation and 850-mb wind vector, Fig. 3b for SW flux, and Fig. 3c for LH flux. This particular time period coincides with the transition of the precipitation center from SCS to NWP (see Figs. 2b,c) and is, hence, well suited for assessing the model performance in reproducing the timing of a critical stage in the monsoon evolution. Both observations (Fig. 3) and model (Figs. 2c,g,k) indicate drying tendencies over the central portion of the SCS as well as increasing rainfall and cyclonic circulation to the northeast of the Philippines. The dry band and anticyclonic flow developing near 30°N is evident in Figs. 2c and 3a. In the PS/WNP domain, the observed patterns for SW and LH fluxes exhibit negative tendencies near 10°–20°N and positive tendencies near 25°–35°N (Figs. 3b,c), in support of the dipolar distribution based on the model results (Figs. 2g,k).

Tendency plots based on observations have also been constructed for periods other than the duration of 20 June–9 July as shown in Fig. 3. The sequence of such observational charts for SW and LH fluxes (not shown) is in general agreement with the model results presented in Figs. 2e–l. The precipitation tendency patterns based on GPCP data (also not shown) are considerably more noisy than the model charts (Figs. 2a–d), and the spatial correspondence between observed and simulated distributions for precipitation is typically weaker than that for the surface fluxes.

4. Temporal development of climatological SCS/WNP monsoon in zonal and meridional directions

To delineate the detailed evolution of the SCS/WNP monsoon, latitudinal averages of various climatological fields are computed at 5-day (pentad) intervals. At a given longitude between 100° and 160°E, these averages are taken over a band with 10° latitudinal width. The northern and southern limits of this band (shown as red segments in Figs. 2a–d) are shifted progressively poleward with increasing longitude so as to accommodate the southwest-to-northeast orientation of the migration path of the wet zone. The pentadal and latitudinal averages are then plotted as a function of time and longitude. Model and observed patterns are shown in Fig. 4 for precipitation and 850-mb wind vector (Figs. 4a,e), SW flux (Figs. 4b,f), LH flux (Figs. 4c,g), and SST (Figs. 4d,h).

In the model atmosphere, the earliest precipitation signal in the domain under consideration appears near 100°–110°E (i.e., southern Indochina) in mid-May (Fig. 4a).

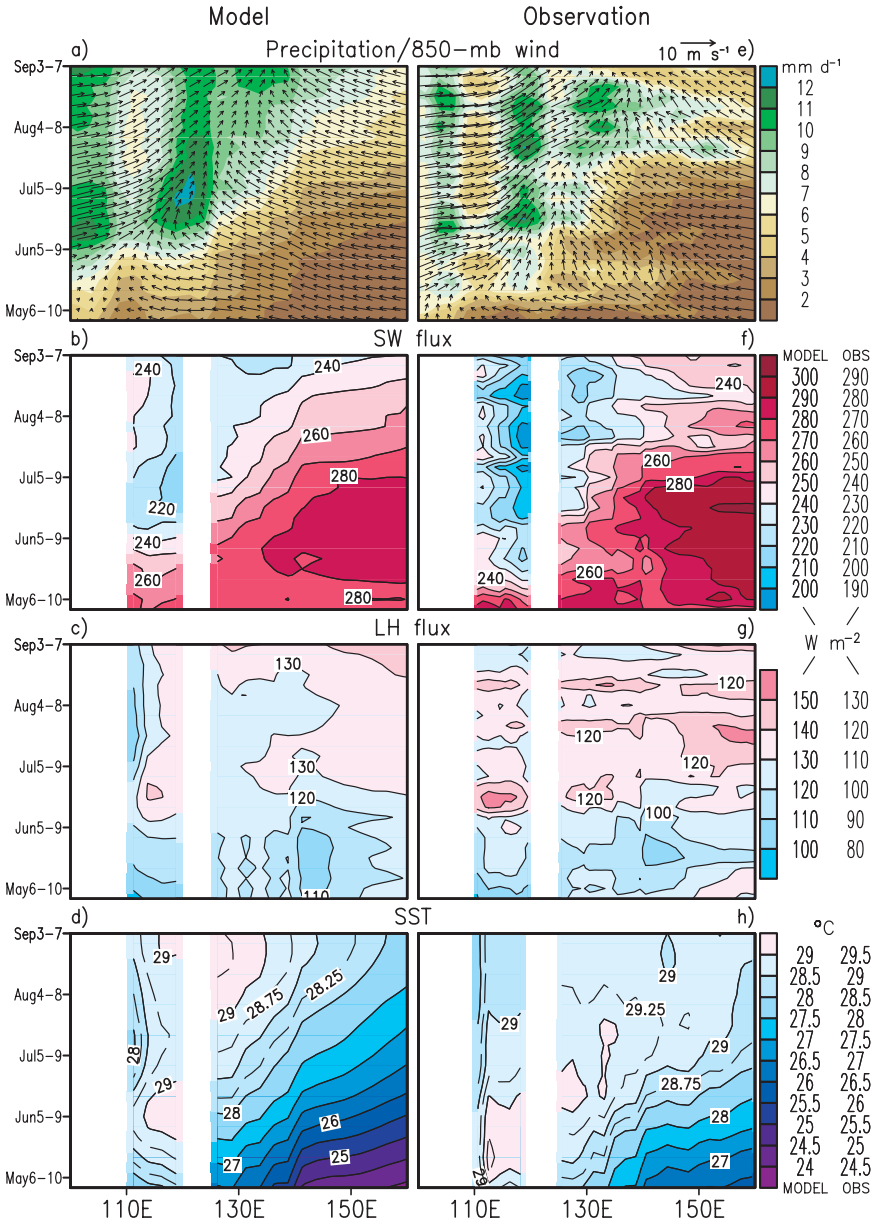

FIG. 4. Variations along the southwest-to-northeast precipitation track in the SCS/PS/WNP region (see red line segments in left panels of Fig. 2) with pentad in the calendar year (ordinate) and longitude (abscissa). At each longitude, averages are taken over the 10° lat span of the track, as delimited by the northern and southern red line segments (see Fig. 2) for that longitude. Results are shown for (first row) precipitation (shading) and 850-mb wind vector [arrows, see scale above (e)], (second row) downward shortwave flux, (third row) upward latent heat flux, and (fourth row) sea surface temperature. Patterns are based on 5-day averages of climatological data from (left) CM2.1 and (right) various observational projects. To accommodate the systematic biases between the model and observations, the range of model values corresponding to given color shade is shifted relative to the range of observational values. Two columns of values (the left for model data, the right for observations) are used to label the scale bars for patterns in the lower three rows. The polarity and magnitude of these offsets reflect the main biases of the simulated values relative to the observations (+10 W m^{-2} for shortwave flux, +20 W m^{-2} for latent heat flux, and −0.5°C for SST). Dashed contours in (d) correspond to values of 28.25°, 28.75°, and 29.25°C. Dashed contours in (h) correspond to values of 28.75° and 29.25°C.

The rainfall increases markedly within 115°–125°E (eastern SCS and the Philippines) in June, whereas the WNP east of 130°E remains dry during this period. The precipitation rate in the latter region intensifies in July–August. The northeastward spread of the precipitation maximum is accompanied by advances of the 850-mb southwesterlies from the SCS to the WNP and the attendant retreat of the easterlies over the WNP.

Arrival of the SCS monsoon in May–June is coincident with increased cloud cover and reduced incoming solar radiation within the 110°–120°E zone. The SW flux over the SCS decreases by 40–50 W m^{-2} in this period (Fig. 4b). The attenuation of SW flux over the PS and WNP occurs noticeably later than the corresponding changes over the SCS. The timing of this development is evidently related to the northeastward march of the precipitation signal over this domain (see Fig. 4a).

The strengthening of the SCS monsoon in May–June results in higher surface wind speeds and an increase in LH flux of about 20–30 W m^{-2} within 110°–120°E during that period (Fig. 4c). The magnitude of the changes in LH flux in the PS and WNP is comparatively weaker.

In accord with the decreasing SW flux and increasing LH flux over the SCS sector during the May–June period, the SST within 110°–120°E rises to a peak in early June and drops gradually in July (Fig. 4d). In contrast, the SST in the PS and WNP continues to increase through the June–July period and attains peak values in mid-August. The results in Fig. 4d portray a sharp contrast between the SST pattern in June, when the surface waters in SCS is relatively warmer than those in PS/WNP, and the corresponding pattern in July–August, when the east–west gradient is reversed.

The essential aspects of the time–space evolution of various model signals in the left column are also discernible in the observed patterns presented in right column. Particularly noteworthy are the northeastward advance of the observed precipitation and southwesterly flow across the SCS/WNP domain during the June–August period (Fig. 4e); the diminishing SW flux over SCS during May–June, and in 125°–135°E about one month later (Fig. 4f); enhancement of the LH flux over the SCS during May–June (Fig. 4g); and reversal of the east–west SST gradient across the SCS and PS/WNP in the course of the summer season (Fig. 4h). The SST maximum and initiation of the wet period in the eastern SCS occurs earlier in the observed atmosphere than in the model simulation. The peak observed precipitation rate and SST in the WNP also take place several pentads earlier than the corresponding model features. The appearance in the simulation of a equatorial Pacific cold tongue that is too strong and extends too far to the west probably contributes to such model biases in the precipitation and SST fields in the WNP (Sperber and Annamalai 2008; Stowasser et al. 2009). The dry zone near 110°E (off the Vietnamese coast), which is partially related to local coastal upwelling (see cold SST at that longitude in Fig. 4h), is more prominent in the observed pattern than in the model atmosphere.

The detailed development in the meridional direction of the monsoon features over WNP is examined in Fig. 5, which shows pentadal data for simulated (Fig. 5a) and observed (Fig. 5b) precipitation and 850-mb wind vector as a function of time and latitude. For a given latitude, averages of these data are taken over the longitudinal zone from 120° to 150°E. In the model atmosphere (Fig. 5a), the axis of the primary rain belt in the WNP sector migrates northward from about 5°N in early June to about 15°N in August. The prevalent 850-mb circulation within this rain belt is seen to switch from an easterly pattern in early summer to a southwesterly pattern in August. In the July–August period, the cyclonic development of the flow pattern in the 10°–25°N zone may be inferred from the counterclockwise turning of the wind vectors when they are scanned from south to north across this zone. Located immediately to the north of the main WNP precipitation belt is a dry region with anticyclonic meridional wind shear (note clockwise turning of the vectors with increasing latitude). The characteristics of this dry zone are closely related to the subtropical ridge over WNP (see Fig. 1). The patterns in Fig. 5a offer additional evidence on the poleward migration of the axis of this anticyclone from about 20°N in June to 35°N in August. During the June–July period, a secondary rainband with prevalent southwesterly flow is discernible to the north of the subtropical high. This precipitation feature is centered near 30°N in June and corresponds to the eastern extension of the mei-yu–baiu front. The timing and location of the principal precipitation and circulation features are similar in simulated (Fig. 5a) and observed (Fig. 5b) patterns. The observed rainfall rates near the mei-yu–baiu front are higher than those simulated by CM2.1, whereas precipitation intensity of the primary WNP rain belt in 5°–20°N in the model is too strong when compared with the observations.

5. Impact of ENSO on the evolution of the SCS/WNP monsoon

Outstanding ENSO events appearing in the CM2.1 simulation are selected using a procedure similar to that adopted in Lau et al. (2008). An index of the SST fluctuations in the central equatorial Pacific is constructed by averaging the monthly SST anomalies over the domain within 5°S–5°N, 120°–170°W. The time series of this index is smoothed by computing 5-month running

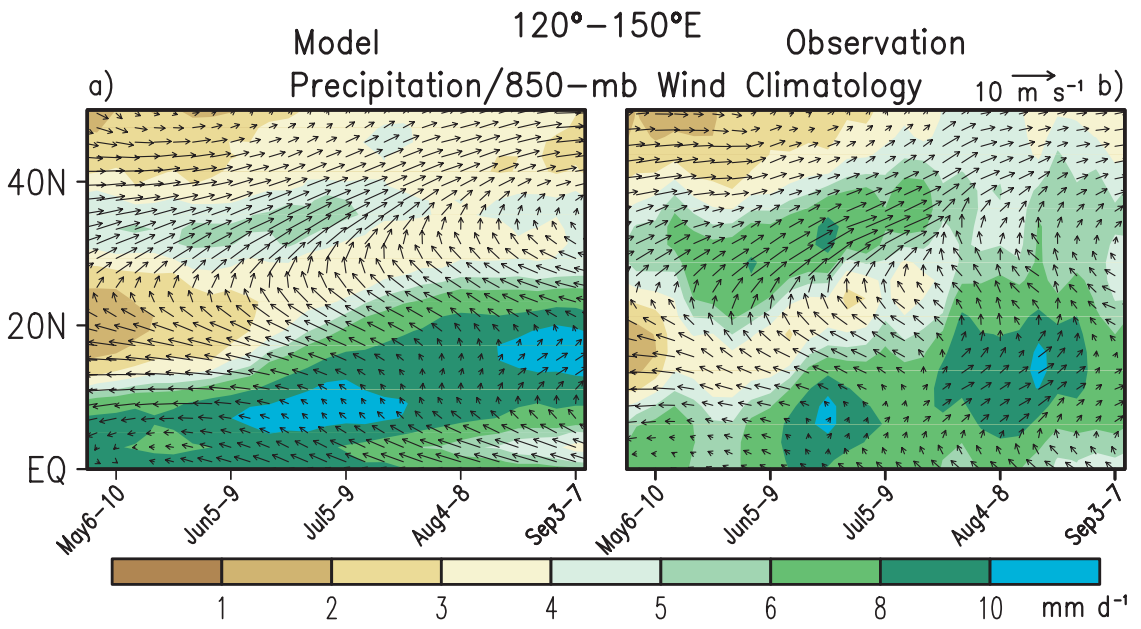

FIG. 5. Variations of longitudinal averages of precipitation (shading) and 850-mb wind vector (arrows) over the 120°–150°E zone with latitude (ordinate) and pentad in the calendar year (abscissa). Patterns are based on 5-day averages of climatological data from (a) CM2.1 and (b) various observational projects [see scale above (b) for 850-mb wind vector].

means. A warm (cold) ENSO event is identified when the SST index exceeds the thresholds of 0.4°C (−0.4°C) for six consecutive months or longer. In a majority of the events that satisfy this criterion, the SST index first reaches the threshold value near the beginning of a given year [hereafter referred as the year of initiation or year(0)]. This index then attains maximum amplitude toward the end of year(0), or the beginning of the following year [hereafter referred as year(1)], and finally falls below the threshold value in the middle or latter half of year(1). Only those events that follow this general evolutionary pattern are chosen.[2] This procedure yields altogether 34 warm events and 45 cold events.[3] We shall henceforth refer to the temporal phase of the ENSO events by using a label that consists of the first three letters of the month for that phase, followed by the year indicator (0 or 1) in parentheses. For instance, May(1) refers to the month of May in year(1).

The general characteristics of ENSO events appearing in the CM2.1 integration are analyzed by Wittenberg et al. (2006). The evolution of ENSO-related atmospheric and oceanic anomalies in this model bears some resemblance to that of the observed features. However, the amplitude of the simulated equatorial SST perturbations is too strong, and the principal ENSO signals are displaced too far west of the observed locations. Joseph and Nigam (2006), Guilyardi (2006), and Annamalai et al. (2007), among others, have also compared the performance of CM2.1 in reproducing various ENSO features and ENSO–monsoon relationships with that of various models developed at other centers. These studies demonstrate that, whereas the CM2.1 captures some aspects of the covariability between ENSO and the Asian monsoon circulation, this and all other models still exhibit considerable systematic errors.

a. Evolution of rainfall over SCS and PS in El Niño and La Niña events

Areal averages of the precipitation rates in various pentads of the calendar year are computed for two individual rectangular sites. The first region (8°–18°N, 115°–120°E; hereafter referred to as site A) lies in eastern SCS. The second region (10°–20°N, 125°–130°E; labeled site B) is located immediately to the east of the

[2] In some instances, the smoothed SST index exceeds the ±0.4°C threshold for more than 16 months. For such cases, if the extremum of this index occurs in the August–December period of a certain year, that year is designated as year(0), and the following year is labeled as year(1); if the extremum occurs in the January–May period of a year, that year is designated as year(1), and the preceding year is referred as year(0). Prolonged events with the index peaking in June–July are discarded owing to ambiguities in assigning the labels of year(0) and year(1) to these events.

[3] The SST index exhibits a weak secular trend of approximately 0.1°C per century within the 200-yr segment of the CM2.1 integration examined here. The groups of warm and cold ENSO events, as identified using the detrended SST index, differ only slightly from the set of 34 warm and 45 cold events considered in this study, which are selected prior to any trend removal.

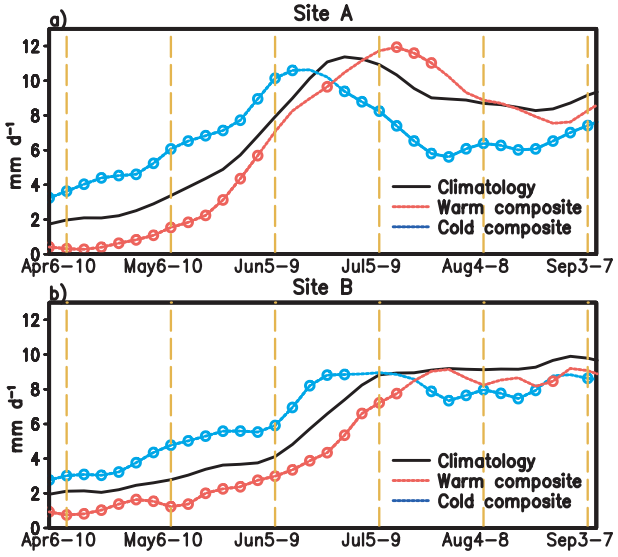

FIG. 6. Time series of the areal average of precipitation over (a) 8°–18°N, 115°–120°E (site A) and (b) 10°–20°N, 125°–130°E (site B), as computed using pentad data from the CM2.1 simulation for 200-yr climatology (black curves), and for year(1) of selected El Niño (red curves) and La Niña (blue curves) events. Those pentads in which the departures of warm (cold) composites of precipitation from climatology surpass the 95% significance level are indicated by red (blue) circles. The boundaries of sites A and B are shown in Fig. 2a.

Philippines. The boundaries of these sites are depicted in Fig. 2a. The pentadal variations of the precipitation are shown for site A in Fig. 6a and site B in Fig. 6b. Results based on 200-yr climatological averages are displayed using black solid curves, whereas the time series based on composites over the data for year(1) of selected 34 warm and 45 cold ENSO events are represented by the red and blue curves, respectively. The composites over El Niño and La Niña events will be referred as warm and cold composites, respectively. We shall focus on the atmospheric and oceanic developments in the boreal warm season of year(1), that is, after the mature phase of typical ENSO episodes.

Comparison of the time series in Fig. 6a with those in Fig. 6b reveals that, for a given data group (i.e., climatology, warm composite, or cold composite), the peak in rainfall rate at site A occurs at about three pentads before the precipitation at site B reaches its maximum level. The temporal lag between the climatological precipitation signals in the SCS and PS (solid black curves in Fig. 6) is consistent with the northeastward development of the monsoon rains across this region. The evidence of an analogous lag between the pair of red curves (warm composite) for sites A and B, as well as between the blue curves (cold composite), implies that the *spatial* evolution of the SCS/WNP monsoon in ENSO years also follows a similar southwest-to-northeast path as the long-term averaged scenario. However, the results in Fig. 6 illustrate that the specific *timing* of this evolution during warm or cold events is markedly different from climatology. In particular, for a given site (A or B), the occurrence of the precipitation peak during warm ENSO events is typically delayed relative to the corresponding climatological peak by several pentads. Conversely, maximum precipitation in cold events precedes the climatological peak by several pentads. These simulated temporal characteristics for the boreal spring and early summer of year(1) are in general agreement with the observational analyses performed by Wu and Wang (2000), who similarly noted a temporal lag (lead) of 2–5 pentads of the monsoon rainfall evolution in SCS/WNP during warm (cold) events versus the climatological development. However, there exists much less supporting observational evidence for the simulated positive (negative) precipitation anomalies over the SCS in Jul(1) of warm (cold) events (see Fig. 6a). The composite charts constructed by Wu and Wang (2000, see their Fig. 7c) using observed outgoing longwave radiation data for Jul(1) indicate only weak precipitation changes over the SCS during ENSO episodes. Anomaly patterns based on GPCP data (not shown) indicate below-normal precipitation over SCS in July of 1983 and 1998, which correspond to year(1) of two recent major El Niño events. This observational result is contrary to the model data presented in Fig. 6a. Linear correlation and regression analyses performed by Xie et al. (2009, see their Figs. 4c and A1d) based on observational data for Jun–Aug(1) yield weak negative (positive) precipitation anomalies over the SCS during warm (cold) events. It is difficult to compare this observational finding with the model result in Fig. 6a since the simulated rainfall anomaly changes sign in the course of the three-month summer season considered in the study of Xie et al. (2009).

b. Asymmetry in El Niño and La Niña development

A key factor in determining the anomalous precipitation pattern in SCS/WNP during ENSO events is the evolution of the SST forcing in the equatorial Pacific. The dependence of the monthly SST anomalies averaged over the 5°S–5°N zone on longitude and temporal phase of the ENSO cycle is portrayed for composites of warm events in Fig. 7a and cold events in Fig. 7b in the CM2.1 simulation.

The distribution in Fig. 7a illustrates that the largest positive SST anomalies in boreal spring and early summer of year(1) are simulated to the east of 150°W during the warm events and that the SST anomalies near and to the west of the date line are relatively weaker in the same period. This tendency for the warm SST anomaly

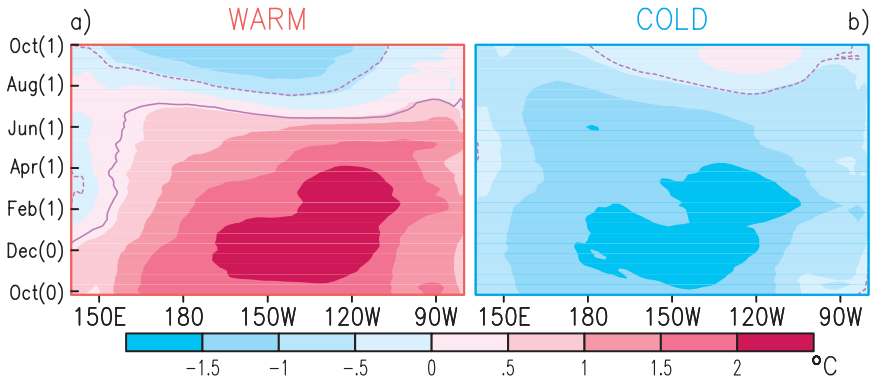

FIG. 7. Variations of latitudinal averages of sea surface temperature anomaly over the 5°S–5°N zone with time (ordinate) and longitude (abscissa) for composites over (a) warm and (b) cold ENSO events. Patterns are based on monthly means from the CM2.1 simulation. Positive (negative) anomaly values at the 95% significance level are indicated by solid (dashed) purple contours.

center to migrate eastward with time during the first half of year(1) is in sharp contrast to the corresponding development in simulated cold events (Fig. 7b). The latter composite indicates westward advancement of the cold anomaly in May(1)–Aug(1), with stronger SST amplitudes near and to the west of the date line and weaker signals east of 120°W.

The above findings on the asymmetries in SST evolution in simulated warm and cold events may be compared with the observational results presented by Larkin and Harrison (2002, their Fig. 8). In support of the model results, the observations also indicate that the anomalous SST extremum in year(1) of warm events is located east of the corresponding feature in cold events, and that the transition from warm to cold phase takes place earlier in year(1) than the transition from cold to warm phase. These asymmetries lead to a relatively more distinct and persistent cold SST anomaly in the western equatorial Pacific during the boreal summer of year(1) in observed La Niña events compared to the warm anomaly in observed El Niño episodes.

Some understanding of the eastward (westward) advance of SST anomalies in simulated warm (cold) events (Fig. 7) may be gained by considering the pertinent terms in the equation for the SST budget, which determines the propagation characteristics of the "SST modes" of ENSO development (e.g., see reviews by Neelin et al. 1998; Wittenberg 2002; Wang and Picaut 2004). In particular, we focus on the contributions of the nonlinear advection terms, $-u'T'_x$ and $-w'T'_z$ (A. T. Wittenberg 2008, personal communication). Here u and w are the surface ocean current speeds in the zonal (x) and vertical (z) directions, respectively, and T_x and T_z are the partial derivatives of the ocean surface temperature T with respect to x and z; the prime represents the anomalous component. During an El Niño event, the anomalous eastward wind stress to the west of the warm SST center leads to anomalous eastward surface current ($u' > 0$) and downwelling ($w' < 0$) (e.g., see Fig. 11 of Neelin et al. 1998). The eastward and downward penetration of warm surface waters during warm events also alter the zonal and vertical temperature gradients, so $T'_x > 0$ and $T'_z < 0$. Hence, $-u'T'_x < 0$ and $-w'T'_z < 0$ to the west of the warm SST anomaly. Cooling at that location is conducive to an eastward tendency of the warm anomaly. An and Jin (2004) have similarly noted the roles of the $-u'T'_x$ and $-w'T'_z$ terms in the eastward migration of the SST anomaly in the outstanding 1982–83 and 1997–98 El Niño events. Conversely, the anomalous westward wind stress to the west of the cold SST center during La Niña is associated with $u' < 0$ and $w' > 0$. The modified distribution of the oceanic temperature gradient is characterized by $T'_x < 0$ and $T'_z > 0$. The terms $-u'T'_x$ and $-w'T'_z$ are again negative to the west of the cold anomaly and therefore lead to westward migration of this SST signal. The contributions of these nonlinear effects to the SST budget are particularly significant during strong ENSO events when large perturbations to the temperature gradients (i.e., T'_x and T'_z) occur. The prominence of eastward (westward) SST propagation during the simulated warm (cold) events (Fig. 7) partially results from the excessive amplitude of the SST variability related to ENSO phenomena in CM2.1 (Wittenberg et al. 2006).

Through arguments analogous to those presented in the preceding paragraph, it can be shown that linear terms in the SST budget equations, such as $-u'\overline{T}_x$ and $-w'\overline{T}_z$, where the overbar denotes time averages, lead to westward propagation of both warm and cold SST anomalies for a basic state with $\overline{T}_x < 0$ and $\overline{T}_z > 0$. Hence, the asymmetric spatial evolution of the warm and

cold events cannot be attributed to these linear terms. The relative importance of the linear and nonlinear terms remains to be quantified by a detailed analysis of the SST budget, which is beyond the scope of this study.

c. *Anomalous circulation and precipitation patterns in warm and cold events*

The anomalous atmospheric patterns associated with the distinctive SST development in the Pacific and Indian Ocean basins during the opposite phases of ENSO are explored in Fig. 8, which shows composite charts for the El Niño (left panels) and La Niña (right panels) events as identified in the CM2.1 simulation. Model anomalies are shown for the months of May(1) (top two rows) and Jul(1) (bottom two rows). Results are presented for SST (shading) and 200-mb velocity potential χ and divergent circulation $\mathbf{V}_\chi$ (contours and arrows, respectively) in Figs. 8a,c,e,g and for precipitation (shading) and 850-mb streamlines in Figs. 8b,d,f,h.

In the May(1) composite of the warm events, the SST pattern in the tropical western Pacific (shading in Fig. 8a) consists of an elongated near-equatorial positive anomaly extending east of ~160°E and a pair of negative anomalies centered near 15°N, 165°E and 10°S, 180°. Warm conditions prevail in the tropical Indian Ocean and southern portion of the SCS. This configuration is similar to observations for this phase of ENSO development (e.g., see Harrison and Larkin 1998; Alexander et al. 2004) except that the simulated Pacific warm anomaly is displaced to the west of its observed location. The above-normal SST in the Indo–western Pacific is partially due to the atmospheric bridge mechanism linking ENSO to these maritime sites (e.g., Klein et al. 1999; Alexander et al. 2004). The corresponding distributions of χ and $\mathbf{V}_\chi$ at 200 mb (contours and arrows in Fig. 8a) indicate anomalous large-scale divergence from warm SST zones over the equatorial Pacific and eastern tropical Indian Ocean. These regions are collocated with enhanced precipitation and anomalous westerlies at 850 mb (Fig. 8b). Large-scale convergence at 200 mb occurs along a broad subtropical belt stretching from the Arabian Sea to 150°W where dry conditions and low-level anticyclonic flows prevail. Situated still farther north of the anomalous ridge over the WNP is a cyclonic cell with its axis located in the 35°–45°N band. This extratropical feature and the subtropical ridge to its south straddle an anomalous westerly or southwesterly zone at 25°–35°N with above-normal precipitation. The pair of circulation cells at 850 mb in subtropical and extratropical North Pacific with opposing vorticity changes is reminiscent of the "Pacific–Japan" teleconnection pattern associated with variations of convective activity over the WNP (Nitta 1987).

Due to the continuous eastward displacement of the SST signal in the boreal summer of year(1) in the simulated warm events and the rapid phase transition from El Niño to La Niña within this period (see Fig. 7a), the positive SST anomaly in the equatorial Pacific is much diminished in Jul(1) (Fig. 8c). The strength and spatial extent of the warm anomaly in the Indian Ocean also decreases from May(1) to Jul(1). On the contrary, the warm conditions in the SCS persist through this period. The altered SST anomaly pattern in Fig. 8c is accompanied by weakened upper-level divergence from the equatorial central Pacific and northern Indian Ocean, a northeastward shift of the 200-mb convergence center (as inferred from the maximum in χ) over WNP, and the prevalence of divergent flows over the SCS. These circulation changes in the upper troposphere are, in turn, associated with a northward shift of the axes of the dry 850-mb subtropical ridge over the WNP and a corresponding poleward migration of the elongated wet zone lying on the northern flank of this ridge. Over most parts of the SCS, the low-level circulation is characterized by anomalous easterlies.

The negative SST anomaly in the equatorial Pacific in May(1) of the composite cold events (Fig. 8e) has a higher amplitude and extends farther to the west than the corresponding positive anomaly in the warm composite (Fig. 8a). Most of the other features in the warm composite for May(1) (Figs. 8a,b) are also discernible in the cold composite (Figs. 8e,f) but with reversed polarity.

In sharp contrast to El Niño development (Figs. 7a and 8c), the negative SST anomaly in cold events retains much of its strength throughout the boreal summer of year(1) and continues to migrate westward in this period (Figs. 7b and 8g). Consequently, the SST pattern in Jul(1) is dominated by negative anomalies throughout the western equatorial Pacific and SCS. Below-normal SST conditions are still evident in the Indian Ocean but with reduced amplitudes. The intensity of the circulation and precipitation anomalies over the SCS and WNP (Figs. 8g,h) is notably higher than that in the warm composites (Figs. 8c,d). An anomalously wet cyclonic center prevails near 30°N, 135°E (Fig. 8h). The dry anomaly situated over southeastern China in May(1) (Fig. 8f) is seen to migrate toward the Korea/southern Japan sector two months later (Fig. 8h).

The westward displacement of the simulated dry anomaly over the equatorial western Pacific in cold events (Fig. 8f) relative to the wet anomaly in warm events (Fig. 8b) is consistent with the observational findings of Hoerling et al. (1997) on the asymmetries between the two opposing phases of ENSO. The simulation of strengthened (weakened) subtropical anticyclone over WNP and mei-yu–baiu activity in year(1) of El Niño (La Niña) events, as illustrated in Fig. 8, is

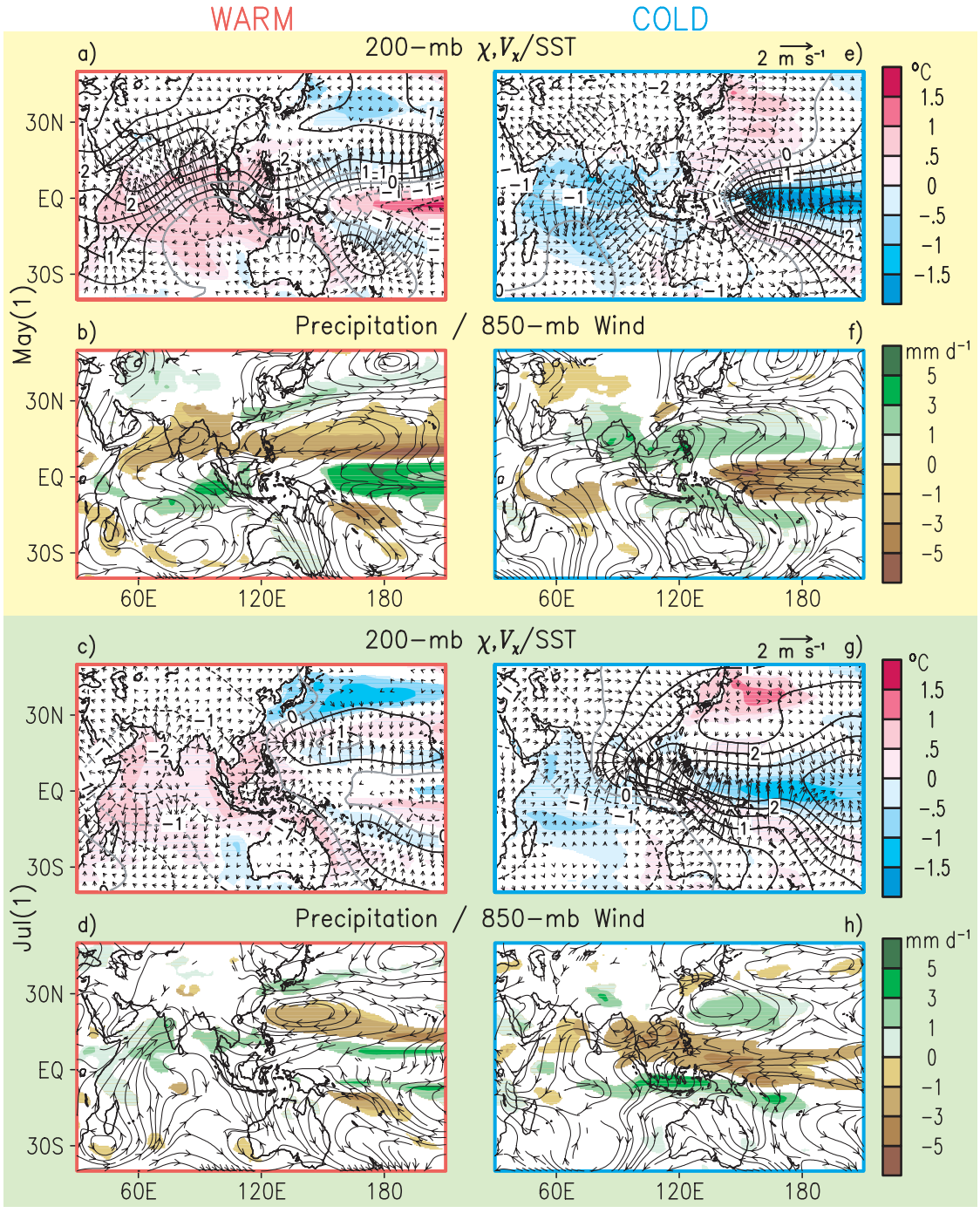

FIG. 8. Distributions of the anomalies of (first row), (third row) 200-mb velocity potential (contours, interval: 0.5 × 10^6 m^2 s^{-1}; solid and dashed contours indicate positive and negative values, respectively) and divergent wind vector [arrows, see scale above (e) and (g)], and SST (shading); and (second row), (fourth row) 850-mb flow field (streamlines) and precipitation (shading). Patterns are based on monthly means from the CM2.1 simulation for composites over the (left) warm (red frames) and (right) cold (blue frames) ENSO events. Results are presented for the periods of May(1) (upper half, with yellow background) and Jul(1) (lower half, with green background). Only those SST and precipitation anomalies that exceed the 95% significance level are depicted with color shading; those locations where the anomalies do not meet this criterion are left blank. Velocity potential anomalies above (below) the 95% significance level are indicated using black (gray) contours. The scale bar used for the color shading in each row is shown at the right edge of that row.

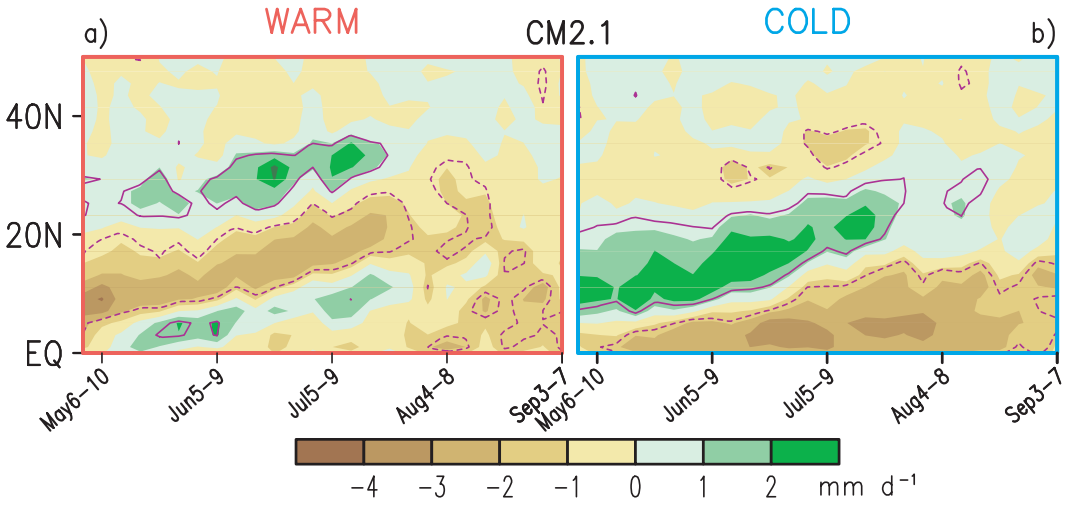

FIG. 9. Variations of longitudinal averages of precipitation anomalies over the 120°–150°E zone with latitude (ordinate) and time in year(1) (abscissa). Patterns are based on 5-day means from the CM2.1 simulation. Results are presented for signals in composite (a) warm (red frame) and (b) cold (blue frame) ENSO events. Positive (negative) anomaly values at the 95% significance level are indicated by solid (dashed) purple contours.

supported by the observational evidence presented by Shen and Lau (1995) and Chang et al. (2000a,b).

The latitudinal development of the major precipitation anomalies in the SCS/WNP sector is examined in greater detail in Fig. 9. The patterns in this figure are based on the methodology used for Fig. 5a, and are shown for the warm (Fig. 9a) and cold (Fig. 9b) composite of the CM2.1 data. The pattern in Fig. 9a is dominated by the poleward migration of two coherent features: a dry anomaly with displacement from about 10°N in May(1) to 20°N in Jul(1) and a wet anomaly advancing from 25°N in May(1) to 35°N in Jul(1). As evident from the maps in Figs. 8b and 8d, the spatial shift of the dry anomaly is closely related to the movement of the anomalous anticyclone in the subtropical WNP, whereas the evolution of the wet anomaly follows that of the westerly belt situated immediately to the north of this anticyclone. Inspection of the anomaly pattern in Fig. 9a and its climatological counterpart in Fig. 5a illustrates that the precipitation anomalies in warm events tend to reinforce the poleward movement of the climatological dry zone in the subtropical WNP and the parallel displacement of the mei-yu–baiu rain belt farther north. The above phenomena are simulated with reversed polarity in cold events (Fig. 9b).

6. Contrasting the effects of remote and local SST forcing on the SCS/WNP monsoon

a. Experimental design

The overall model evidence presented in Fig. 8 suggests that the circulation and rainfall anomalies in the SCS/WNP sector are linked in varying degrees to remote forcing associated with SST changes in the tropical Pacific and Indian Oceans as well as to local air–sea interactions within SCS/WNP itself. Various investigators have previously noted the influences on the East Asian monsoon due to SST variability in the Pacific (e.g., Chang et al. 2000a,b; Wang et al. 2000; Wu and Wang 2000) and Indian Ocean (e.g., Annamalai et al. 2005; Yang et al. 2007; Xie et al. 2009) sectors. These relationships are further explored in this study by direct experimentation with the atmospheric component of CM2.1. This set of integrations entails the prescription of time-varying SST anomalies at the lower boundary of this atmospheric model (AM2.1). The monthly SST data used in this procedure are obtained from composites of warm and cold events identified in the 200-yr simulation with the fully coupled CM2.1 (see details in section 5). In each integration, the prescription of SST composite data is performed for the 21-month duration from Mar(0) to Nov(1). Integrations are conducted separately for the composite warm and cold events and for each of the following prescription domains.[4]

[4] For each of the experiments in this list, the oceanic grid points lying outside of the respective SST prescription domain are constrained to follow the climatological seasonal cycle, as given by the 200-yr average of the CM2.1 simulation. To ensure a smooth transition from the region where SST composite data are applied to the region subjected to climatological conditions, the composite data are linearly interpolated to the climatological values over a taper zone with a latitudinal or longitudinal width of about 4°.

- The tropical Pacific extending from 15°S to 15°N and from 135°E to the American coasts. The western portion of this domain is depicted using red borders in Figs. 10e and 11e. This integration is hereafter referred as the ENSO experiment.
- The Indian Ocean extending from 30°S to the South Asian coasts and to the southern portion of the Indonesian Archipelago. This domain is depicted using red borders in Figs. 10f and 11f. This integration is hereafter referred as the IO experiment.
- The SCS/WNP sector, extending from the East Asian coast to 135°E within the 5°S–15°N band and to 180° within the 15°–30°N band. This domain is depicted using red borders in Figs. 10g and 11g. This integration is hereafter referred as the SCS/WNP experiment.
- Combination of the three domains used in the ENSO, IO, and SCS/WNP experiments. The western portion of this domain is depicted using red borders in Figs. 10h and 11h. This integration is hereafter referred as the ENSO + IO + SCS/WNP experiment.

In addition to the above experiments, a 30-yr integration with AM2.1 has been completed with the climatological seasonal cycle of the SST field being inserted at grid points throughout the World Ocean. This simulation is hereafter referred as the CLIMO experiment. For each of the four prescription domains considered here, the 21-month integrations are repeated 30 times with initial states being furnished by output from the CLIMO experiment for individual years. The suite of experiments with time-varying SST forcing requires integration over a total of four (prescribed domains) $\times$ 2 (warm and cold composites) $\times$ 30 (ensemble members) $\times$ 21 (duration) = 5040 months. In the following presentations, the anomalous response of AM2.1 to composite SST forcing prescribed in a specific domain (i.e., ENSO, IO, SCS/WNP, or ENSO + IO + SCS/WNP) is obtained by subtracting the 30-yr average of the CLIMO simulation from the 30-member ensemble mean of the respective experiment.

It should be emphasized that this experimental design is suited for attributing various atmospheric signals to a given SST forcing, but provides no information on the origin of the SST forcing, and does not take into consideration the feedback effects of the atmospheric response on various ocean fields. Douville (2005), Copsey et al. (2006), and other investigators have pointed out the limitations of sensitivity experiments with prescribed SST forcing in reproducing the two-way interactions occurring within the atmosphere–ocean system. The inferences drawn from the suite of AM2.1 integrations described in this section are also dependent on the fidelity of the ENSO-related SST variations as produced by CM2.1. As mentioned in section 5, this model exhibits biases in the amplitude and spatial pattern of such SST anomalies.

b. Response patterns to SST forcings in equatorial Pacific, Indian Ocean, and SCS/WNP

The departures of χ (contours) and $\mathbf{V}_\chi$ (arrows) at 200 mb and precipitation (shading), as generated in the ENSO, IO, SCS/WNP, and ENSO + IO + SCS/WNP experiments from the corresponding fields simulated in the CLIMO run, are displayed in Fig. 10 for May(1) and in Fig. 11 for Jul(1). Responses to the warm (cold) composite SST forcing are shown in the left (right) panels.

In May(1) the atmospheric responses to the SST forcings in the tropical Pacific and Indian Oceans, as illustrated in the ENSO and IO experiments (Figs. 10a,b,e,f), are notably stronger than the response to the SST changes in the SCS/WNP sector (Figs. 10c,g). Over the SCS/WNP region and for a given ENSO polarity (El Niño or La Niña), the divergent circulation responses to remote ENSO and IO influences tend to oppose the responses to local SST forcing within SCS/WNP. The response in the ENSO + IO + SCS/WNP experiment (Figs. 10d,h) is more similar to the sum of the responses in the ENSO and IO experiments than to the response in the SCS/WNP experiment.

The sum of the responses (not shown) to SST forcings in ENSO, IO, and SCS/WNP, as obtained by adding the data in Figs. 10a–c for warm events and in Figs. 10e–g for cold events, bears a strong resemblance to the response patterns to the combined ENSO, IO, and SCS/WNP forcings, shown in Figs. 10d,h. This finding implies that the net response to the SST anomalies imposed in the ENSO, IO, and SCS/WNP regions may be viewed as the linear superposition of the individual responses to these three separate sites. The patterns in Figs. 10d,h also exhibit a considerable correspondence with warm and cold composites based on output from the fully coupled simulation (Figs. 8a,b,e,f). This favorable comparison between the CM2.1 and AM2.1 patterns indicates that the meteorological signals generated in the coupled scenario of CM2.1 in the boreal summer of year(1) may be viewed primarily as the response of the atmosphere to concurrent SST conditions. In such situations where air–sea coupling is dominated by the oceanic forcing of the atmosphere, the AM2.1 model would serve as a useful tool for diagnosing the relative roles of different SST anomalies in generating atmospheric changes related to ENSO.

The spatial correspondence between the response patterns in various AM2.1 and CM2.1 experiments, as described in the preceding paragraph, is quantified by computation of spatial correlation coefficients (SCC)

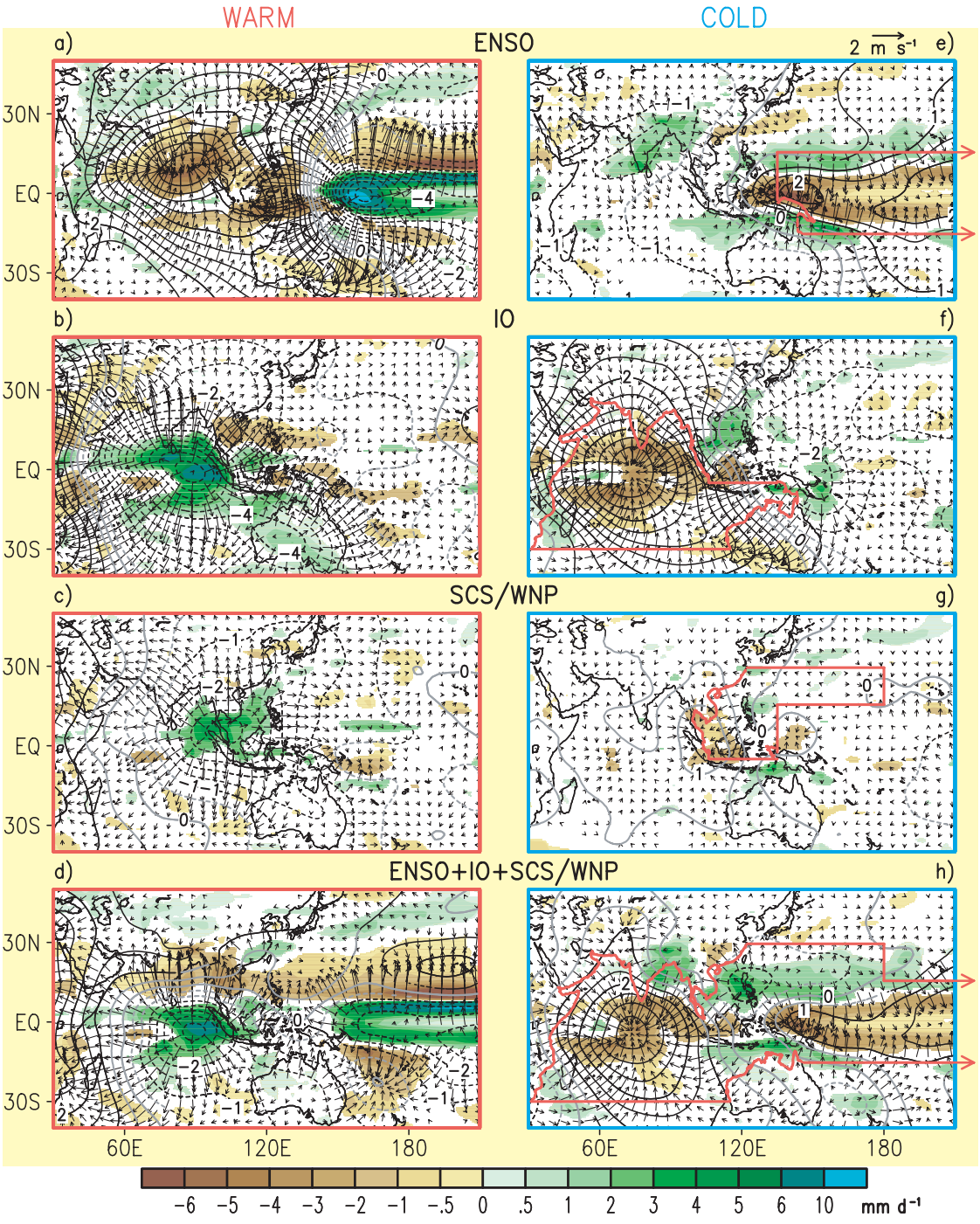

FIG. 10. Distributions of the anomalies of 200-mb velocity potential (contours, interval: 0.5×10^6 m^2 s^{-1}; solid and dashed contours indicate positive and negative values, respectively) and divergent wind vector (arrows) and precipitation (shading). Patterns are based on responses of AM2.1 to composite (left) warm (red frames) and (right) cold (blue frames) SST forcings in May(1). Responses to forcings in the ENSO, IO, SCS/WNP, and ENSO + IO + SCS/WNP experiments are displayed in the first, second, third, and fourth rows, respectively. Only those precipitation anomalies that exceed the 90% significance level are depicted with color shading; those locations where the anomalies do not meet this criterion are left blank. Velocity potential anomalies above (below) the 95% significance level are indicated using black (gray) contours. The scale bar used for the color shading in all panels is shown at the bottom. The scale for plotting the wind vectors in all panels is shown at the upper right of (e). The red borders in right panels [(e)–(g)] indicate the domain for prescription of anomalous SST forcing in the respective experiment. Note that the eastern portion of the forcing domain for the ENSO and ENSO + IO + SCS/WNP experiments extends all the way to the American coasts.

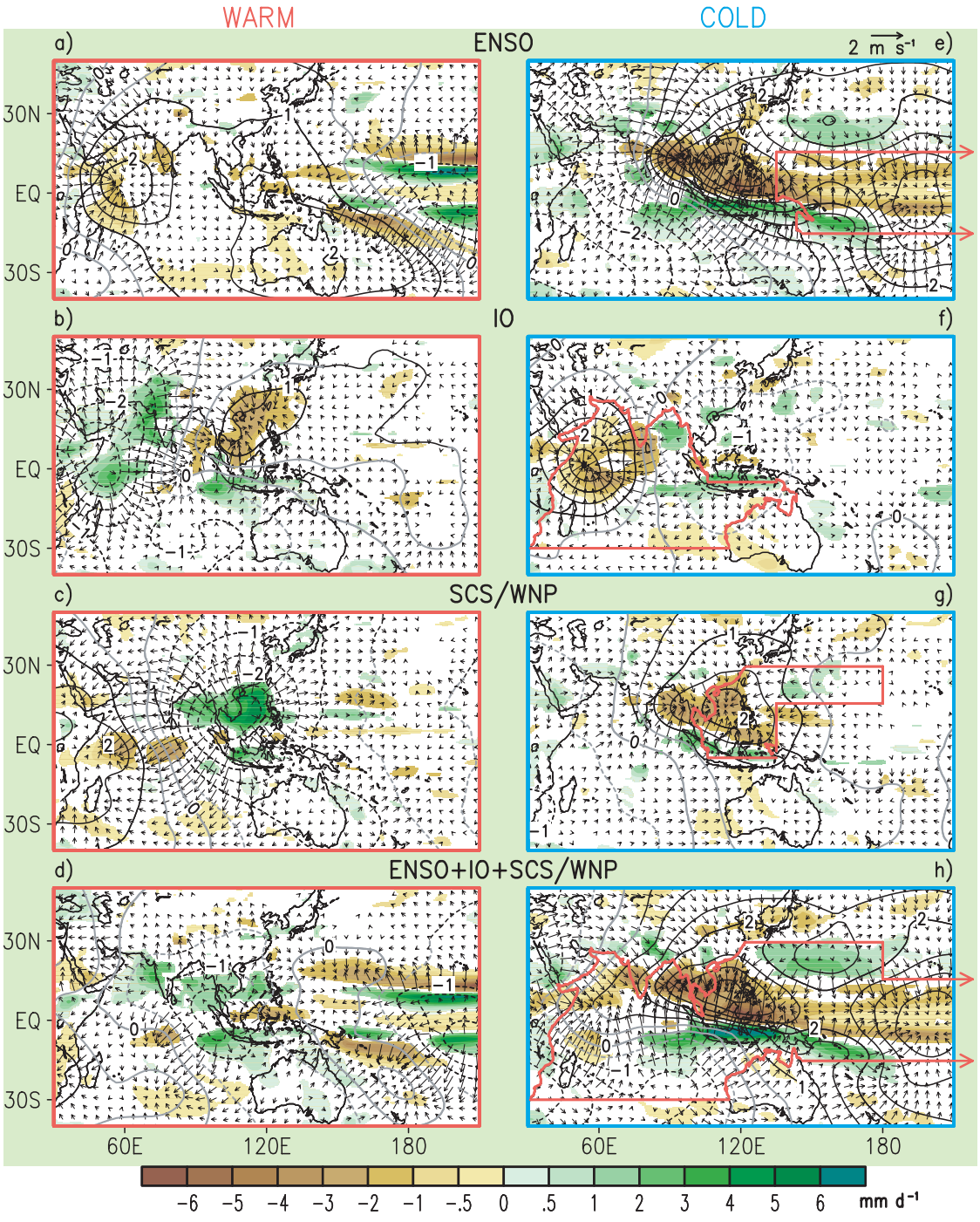

FIG. 11. As in Fig. 10 but for responses to sea surface temperature forcings in Jul(1).

between the anomalous precipitation field in the ENSO + IO + SCS/WNP experiment and the corresponding field in the ENSO, IO, SCS/WNP experiments; linear sums of various pairings among the ENSO, IO, and SCS/WNP experiments; and the CM2.1 simulation. The results for warm and cold events in May(1) are displayed in the left half of Table 1. These statistics confirm the strong resemblance among the precipitation features in the ENSO + IO + SCS/WNP; ENSO; IO; sum of ENSO and IO; sum of ENSO, IO, and SCS/WNP; and CM2.1 experiments. It is also noteworthy that the precipitation response in SCS/WNP (third row in left half of the table) bears a much weaker spatial correlation with that in ENSO + IO + SCS/WNP than the corresponding responses in

TABLE 1. Spatial correlation coefficients between the anomalous precipitation pattern in the ENSO + IO + SCS/WNP experiment and the corresponding responses in the ENSO experiment; IO experiment; SCS/WNP experiment; linear sum of the responses in the ENSO and IO experiments; linear sum of ENSO and SCS/WNP experiments; linear sum of the IO and SCS/WNP experiments; linear sum of the ENSO, IO, and SCS/WNP experiments; and composites of ENSO events simulated by CM2.1. Results are shown separately for May(1) and Jul(1) and for warm and cold ENSO events. Computations are based on the domain of 5°–30°N, 100°–160°E. Statistical significance of the SCC is assessed using a procedure similar to that outlined in footnote 4 of Lau et al. (2008). Altogether 150 samples are drawn from the 200-yr output of the CM2.1 integration, with each sample consisting of 30 months that are randomly chosen. SCC are then computed between all possible (11 175) pairings of these 30-month averages. Threshold values for various percentiles of this population of SCC are noted. SCC values that surpass the thresholds for the 95th and 99th percentiles are indicated using bold italic and underlined bold italic, respectively.

	May(1)		Jul(1)	
	Warm event	Cold event	Warm event	Cold event
ENSO	***0.57***	***0.69***	0.17	***0.95***
IO	***0.72***	***0.46***	−0.26	−0.04
SCS/WNP	0.26	0.34	***0.76***	***0.84***
Sum of ENSO and IO	***0.78***	***0.85***	−0.11	***0.84***
Sum of ENSO and SCS/WNP	***0.62***	***0.67***	***0.81***	***0.95***
Sum of IO and SCS/WNP	***0.67***	***0.58***	***0.71***	***0.76***
Sum of ENSO, IO and SCS/WNP	***0.82***	***0.83***	***0.74***	***0.92***
CM2.1	***0.67***	***0.88***	***0.74***	***0.92***

ENSO or IO (first and second rows). The combination of the responses in the ENSO and IO runs (fourth row) yields a relatively higher SCC with ENSO + IO + SCS/WNP than the combinations of ENSO and SCS/WNP or IO and SCS/WNP (fifth and sixth rows).

In Jul(1) of warm events, the remote influence of the equatorial Pacific SST forcing on the atmospheric conditions near the SCS and western Pacific is much reduced (Fig. 11a). On the other hand, the sustained SST warming in the SCS/WNP sector leads to upper-level divergence and above-normal precipitation in that region (Fig. 11c). This local response to SCS/WNP warming is partially offset by the remote response to the positive SST anomaly over the western IO (Fig. 11b). The forcing in the SCS/WNP domain apparently makes a much stronger contribution to the total response in the ENSO + IO + SCS/WNP experiment (Fig. 11d) than in May(1) (see Figs. 10c,d). The model findings support the notion that the delay in the onset of the SCS/WNP monsoon during warm events (Fig. 6) is the consequence of the following chain of events: subsidence and below-normal precipitation over sites A and B induced remotely by positive SST forcing in the tropical Pacific and Indian Oceans in May(1), continued warmth of the surface waters in the SCS and WNP due to increased SW flux through the May(1)–Jul(1) period, and enhanced precipitation responding locally to this positive SST anomaly in Jul(1). As noted in section 5a, further observational analyses are needed to ascertain the nature of the precipitation anomaly over SCS/WNP in Jul(1) in the real atmosphere. A stronger remote response in the real atmosphere to warming in the western Indian Ocean than is simulated in IO (Fig. 11b) could result in a net dry anomaly over the SCS in the observational record for Jul(1) during warm events.

The response patterns of the ENSO and SCS/WNP experiments for Jul(1) of the La Niña events (Figs. 11e,g) tend to reinforce each other in the SCS/WNP region, with upper-level convergent flow and negative precipitation anomalies being induced by both the persistent cold SST anomaly in the western equatorial Pacific and the local cold conditions due to the effects of the atmospheric bridge (see Klein et al. 1999). The response over SCS/WNP to remote SST cooling in the western Indian Ocean (Figs. 8g and 11f) is relatively weaker. The dominant cooperation between the forcings in ENSO and SCS/WNP leads to an enhanced convergence and dry response in the ENSO + IO + SCS/WNP experiment (Fig. 11h).

The spatial correlation coefficient between the precipitation response pattern for Jul(1) in the ENSO + IO + SCS/WNP experiment and that in various other experiments are listed in the right half of Table 1. These results further illustrate the much larger contribution of the SCS/WNP forcing to the total response in Jul(1) as compared to May(1) (third row). Conversely, the effects of the SST forcing in the IO (both warm and cold events) and in ENSO (warm events) are much weaker in Jul(1) than in May(1) (first and second rows). For cold events, the combination of ENSO and SCS/WNP forcings (fifth row) yields the highest SCC with the total response compared with other pairings (fourth and sixth rows). The strong correspondence between the pattern in ENSO + IO + SCS/WNP with the linear sum of the individual responses in ENSO, IO, and SCS/WNP (seventh row) and between the AM2.1 and CM2.1 results

(eighth row), as noted previously for May(1), is equally evident in the Jul(1) data.

7. Summary and discussion

The mechanisms contributing to the climatological northeastward advance of the summer maritime monsoon across the SCS/WNP sector are diagnosed on the basis of an extended simulation with a coupled atmosphere–ocean GCM. In the May–June period, the arrival of the monsoon rain over SCS brings about increased cloud cover and surface wind speed over that region. These changes lead to reduced downward SW flux and enhanced upward LH flux at the ocean surface (Figs. 2f,j). Both of these effects result in local SST cooling. At the same time, the waters in the PS and WNP continue to warm, mainly due to the prevalent dry and clear-sky conditions and, hence, stronger SW fluxes (relative to those over SCS) in that sector. As a consequence of this east–west contrast in surface heating, the prevalent thermal gradient in early summer (with the SST in the SCS being warmer than that in the WNP) is reversed by July (with the WNP warmer than the SCS) (Fig. 4d). The precipitation center follows the movement of the site of maximum SST so that rainfall rates over the WNP increase markedly in July and August. The positive precipitation changes over the WNP are concomitant with easterly or northeasterly tendencies near 30°N, which oppose the prevalent southwesterly airstream that supplies moisture to the mei-yu–baiu rainband. The reduced mei-yu–baiu activity near 30°N in July leads to increased SW flux and oceanic warming at that site. The resultant pattern of SST tendency in the WNP is conducive to northward movement of the monsoon rainfall in this region (Fig. 5a).

The relationships between ENSO and the development of the summer monsoon over SCS/WNP are explored by partitioning the output from CM2.1 according to El Niño and La Niña events. This composite analysis is augmented by integrations with AM2.1 subjected to SST forcing at different strategic sites. The asymmetric nature of warm and cold phases of ENSO has a strong impact on the strength and location of the SST forcing in the equatorial Pacific (Fig. 7). The cumulative model evidence indicates that both the remote forcings from the tropical Pacific and Indian Oceans and the local SST within the SCS/WNP domain play substantial roles in the variability of the SCS/WNP during the summer after the mature stage of ENSO. In warm events, precipitation over the SCS and WNP is suppressed in May mainly due to large-scale subsidence forced remotely by SST anomalies residing in the tropical Pacific and Indian Oceans (Figs. 10a,b). These remote forcings weaken considerably in the course of the summer season so that their influence on the SCS/WNP monsoon are much diminished by July (Figs. 11a,b). Meanwhile, the warm anomaly within SCS persists through the May–July period and plays an ascending role in the latter half of summer (Fig. 11c). This sequence of atmospheric responses to remote and local SST changes results in a delay in the arrival of the precipitation maximum over the SCS relative to model climatology (Fig. 6a) and prolonged mei-yu–baiu activity at WNP near 30°N (Fig. 9a).

Over the SCS and WNP, the ascent forced remotely by SST changes in the tropical Pacific and Indian Oceans during May(1) of cold events (Figs. 10e,f) more than compensates the subsidence due to local SST forcing (Fig. 10g), thus leading to low-level cyclonic and positive precipitation anomalies over the SCS and WNP in this period (Fig. 8f). The cold anomaly in the equatorial Pacific persists and penetrates farther westward during May(1)–Jul(1) (Fig. 7b), so SST forcings in the equatorial Pacific and SCS/WNP domains cooperate with each other in generating subsidence and below-normal rainfall over SCS in Jul(1) (Figs. 11e,g). The remote forcing of the tropical Indian Ocean on the circulation and precipitation fields over SCS is relatively weak in Jul(1) (Fig. 11f). These changes during cold events account for the occurrence of the precipitation peak over the SCS in early summer (Fig. 6a). Weakening of the climatological anticyclone over the subtropical WNP (Figs. 8f,h) also leads to decreased intensity of the mei-yu–baiu rainband in the 120°–150°E sector during cold events (Fig. 9b).

We have devoted our attention to the impacts of ENSO on the variability of the SCS/WNP monsoon in the summer of year(1), that is, several months *after* typical El Niño and La Niña events have reached their peak strength. Diagrams analogous to Figs. 6 and 9 have been plotted using model data for year(0). The latter results (not shown) indicate that most of the precipitation anomalies in the SCS/WNP region are less distinctive or organized than their counterparts in year(1). The summer of year(0) corresponds to the developing stage of typical ENSO events in CM2.1. The SST anomalies in the SCS/WNP sector are not yet established by the atmospheric bridge mechanism. The feeble atmospheric signals in SCS/WNP during the summer of year(0) may partially be attributed to the weak remote and local SST forcings in this phase of ENSO development.

Both the excessive ENSO intensity and the spurious shift of the ENSO forcing toward the SCS/WNP region in the CM2.1 simulation, as noted by Wittenberg et al. (2006), may result in too much influence of ENSO on the SCS/WNP monsoon. As noted at the conclusion of section 5b, the strength of ENSO events may also affect the propagation characteristics of the SST anomalies,

which are a key consideration for determining monsoon development over SCS/WNP (see section 6). In view of the model bias in overestimating the amplitude of ENSO, the relationship between the SCS/WNP monsoon and ENSO, as delineated from the model analyses in sections 5 and 6, may be applicable especially to strong ENSO events. Attempts to confirm these relationships by observations are hampered by the limited number of strong ENSO episodes in the data record.

Wu and Wang (2001) have emphasized that the observed northeastward development of the summer monsoon over the SCS and WNP does not proceed smoothly with the slow seasonal cycle of SW and SST forcing but is, instead, accomplished by a succession of abrupt advances of monsoon rainfall. These authors proposed that the ''multistage'' character of the observed SCS/WNP monsoon onset primarily results from the superposition of the seasonal cycle and the wet phase of the climatological intraseasonal oscillations (ISO) residing in this region (Wang and Xu 1997). The latter phenomenon has a typical period of about 30 days, and is phase locked with the seasonal cycle, with wet phases occurring in mid-May, mid-June, and late July. The timing of these three consecutive wet phases of the ISO in relation to the seasonal march of the background state favorable for convective activity is a key factor for the sudden onsets over the SCS, PS, and the northeastern portion of WNP, respectively. The present model study is focused on the slow seasonal component of evolution of the atmospheric and oceanic environment. Determination of the extent to which the abrupt nature of the observed monsoon onsets can be mimicked by CM2.1, and understanding of the possible role of ISO in the climatological behavior and variability of the SCS/WNP monsoon, require further diagnosis of the model output.

Acknowledgments. We thank Andrew Wittenberg for several instructive discussions on the dynamical mechanisms affecting ENSO evolution and for providing detailed comments on a preliminary draft of this manuscript. Supportive and insightful remarks on various drafts have also been kindly offered by Isaac Held and Renguang Wu.

REFERENCES

Adler, R. F., and Coauthors, 2003: The Version-2 Global Precipitation Climatology Project (GPCP) monthly precipitation analysis (1979–present). *J. Hydrometeor.,* **4,** 1147–1167.

Alexander, M. A., N.-C. Lau, and J. D. Scott, 2004: Broadening the atmospheric bridge paradigm: ENSO teleconnections to the tropical West Pacific-Indian Oceans over the seasonal cycle and to the North Pacific in summer. *Earth's Climate: The Ocean-Atmosphere Interaction, Geophys. Monogr.,* Vol. 147, Amer. Geophys. Union, 85–103.

An, S.-L., and F.-F. Jin, 2004: Nonlinearity and asymmetry of ENSO. *J. Climate,* **17,** 2399–2412.

Annamalai, H., P. Liu, and S.-P. Xie, 2005: Southwest Indian Ocean SST variability: Its local effect and remote influence on Asian monsoons. *J. Climate,* **18,** 4150–4167.

——, K. Hamilton, and K. R. Sperber, 2007: The South Asian summer monsoon and its relationship with ENSO in the IPCC AR4 simulations. *J. Climate,* **20,** 1071–1092.

Beljaars, A. C. M., 1995: The parameterization of surface-fluxes in large-scale models under free convection. *Quart. J. Roy. Meteor. Soc.,* **121,** 255–270.

Chang, C.-P., Ed., 2004: *East Asian Monsoon*. World Scientific Series on Meteorology of East Asia, Vol. 2, World Scientific, 564 pp.

——, Y. Zhang, and T. Li, 2000a: Interannual and interdecadal variations of the East Asian summer monsoon and tropical Pacific SSTs. Part I: Roles of the subtropical ridge. *J. Climate,* **13,** 4310–4325.

——, ——, and ——, 2000b: Interannual and interdecadal variations of the East Asian summer monsoon and tropical Pacific SSTs. Part II: Meridional structure of the monsoon. *J. Climate,* **13,** 4326–4340.

Copsey, D., R. Sutton, and J. R. Knight, 2006: Recent trends in sea level pressure in the Indian Ocean region. *Geophys. Res. Lett.,* **33,** L19712, doi:10.1029/2006GL027175.

Delworth, T. L., and Coauthors, 2006: GFDL's CM2 global coupled climate models. Part I: Formulation and simulation characteristics. *J. Climate,* **19,** 643–674.

Ding, Y., 2004: Seasonal march of the East Asian summer monsoon. *East Asian Monsoon,* C.-P. Chang, Ed., World Scientific Series on Meteorology of East Asia, Vol. 2, World Scientific, 30–53.

——, and J. C. L. Chan, 2005: The East Asian summer monsoon: An overview. *Meteor. Atmos. Phys.,* **89,** 117–142.

Douville, H., 2005: Limitations of time-slice experiments for predicting regional climate change over South Asia. *Climate Dyn.,* **24,** 373–391.

GFDL Global Atmospheric Model Development Team, 2004: The new GFDL global atmosphere and land model AM2/LM2: Evaluation with prescribed SST simulations. *J. Climate,* **17,** 4641–4673.

Gill, A. E., 1980: Some simple solutions for heat-induced tropical circulation. *Quart. J. Roy. Meteor. Soc.,* **106,** 447–462.

Griffies, S. M., M. J. Harrison, R. C. Pacanowski, and A. Rosati, 2003: A technical guide to MOM4. GFDL Ocean Group Tech. Rep. 5, NOAA/Geophysical Fluid Dynamics Laboratory, Princeton, NJ, 295 pp.

Guilyardi, E., 2006: El Niño–mean state–seasonal cycle interactions in a multi-model ensemble. *Climate Dyn.,* **26,** 329–348, doi:10.1007/s00382-005-0084-6.

Harrison, D. E., and N. K. Larkin, 1998: El Niño–Southern Oscillation sea surface temperature and wind anomalies, 1946–1993. *Rev. Geophys.,* **36,** 353–400.

Hoerling, M. P., A. Kumar, and M. Zhong, 1997: El Niño, La Niña, and the nonlinearity of their teleconnections. *J. Climate,* **10,** 1769–1786.

Huffman, G. J., and Coauthors, 1997: The Global Precipitation Climatology Project (GPCP) combined precipitation dataset. *Bull. Amer. Meteor. Soc.,* **78,** 5–20.

Joseph, R., and S. Nigam, 2006: ENSO evolution and teleconnections in IPCC's twentieth-century climate simulations: Realistic representation? *J. Climate,* **19,** 4360–4377.

Klein, S. A., B. J. Soden, and N.-C. Lau, 1999: Remote sea surface temperature variations during ENSO: Evidence for a tropical atmospheric bridge. *J. Climate,* **12,** 917–932.

Larkin, N. K., and D. E. Harrison, 2002: ENSO warm (El Niño) and cold (La Niña) event life cycles: Ocean surface anomaly patterns, their symmetries, asymmetries, and implications. *J. Climate,* **15,** 1118–1140.

Lau, N.-C., and M. J. Nath, 2003: Atmosphere–ocean variations in the Indo-Pacific sector during ENSO episodes. *J. Climate,* **16,** 3–20.

——, A. Leetmaa, and M. J. Nath, 2008: Interactions between the responses of North American climate to El Niño–La Niña and to the secular warming trend in the Indian–western Pacific Oceans. *J. Climate,* **21,** 476–494.

Lin, S.-J., 2004: A ''vertically Lagrangian'' finite-volume dynamical core for global models. *Mon. Wea. Rev.,* **132,** 2293–2307.

Milly, P. C. D., and A. B. Shmakin, 2002: Global modeling of land water and energy balances. Part I: The land dynamics (LaD) model. *J. Hydrometeor.,* **3,** 283–299.

Murakami, T., and J. Matsumoto, 1994: Summer monsoon over the Asian continent and western North Pacific. *J. Meteor. Soc. Japan,* **72,** 719–745.

Neelin, J. D., D. S. Battisti, A. C. Hirst, F.-F. Jin, Y. Wakata, T. Yamagata, and S. E. Zebiak, 1998: ENSO theory. *J. Geophys. Res.,* **103,** 14 262–14 290.

Nitta, T., 1987: Convective activities in the tropical western Pacific and their impact on the Northern Hemisphere summer circulation. *J. Meteor. Soc. Japan,* **65,** 373–390.

Reynolds, R. W., and T. M. Smith, 1994: Improved global sea surface temperature analyses using optimum interpolation. *J. Climate,* **7,** 929–948.

Shen, S., and K.-M. Lau, 1995: Biennial oscillation associated with the East Asian summer monsoon and tropical sea surface temperatures. *J. Meteor. Soc. Japan,* **73,** 105–124.

Sperber, K. R., and H. Annamalai, 2008: Coupled model simulations of boreal summer intraseasonal (30-50 day) variability. Part 1: Systematic errors and caution on use of metrics. *Climate Dyn.,* **31,** 345–372.

Stowasser, M., H. Annamalai, and J. Hafner, 2009: Response of the South Asian summer monsoon to global warming: Mean and synoptic system. *J. Climate,* **22,** 1014–1036.

Ueda, H., and T. Yasunari, 1996: Maturing process of the summer monsoon over the western North Pacific—A coupled ocean/atmosphere system. *J. Meteor. Soc. Japan,* **74,** 493–508.

——, ——, and R. Kawamura, 1995: Abrupt seasonal change of large-scale convective activity over the western Pacific in the northern summer. *J. Meteor. Soc. Japan,* **73,** 795–809.

Uppala, S. M., and Coauthors, 2005: The ERA-40 Re-Analysis. *Quart. J. Roy. Meteor. Soc.,* **131,** 2961–3012.

Wang, B., 1994: Climatic regimes of tropical convection and rainfall. *J. Climate,* **7,** 1109–1118.

——, Ed., 2006: *The Asian Monsoon*. Springer-Praxis, 787 pp.

——, and X. Xu, 1997: Northern Hemisphere summer monsoon singularities and climatological intraseasonal oscillation. *J. Climate,* **10,** 1071–1085.

——, and LinHo, 2002: Rainy season of the Asian–Pacific summer monsoon. *J. Climate,* **15,** 386–398.

——, R. Wu, and X. Fu, 2000: Pacific–East Asian teleconnection: How does ENSO affect East Asian climate? *J. Climate,* **13,** 1517–1536.

Wang, C., and J. Picaut, 2004: Understanding ENSO physics: A review. *Earth's Climate: The Ocean-Atmosphere Interaction, Geophys. Monogr.,* Vol. 147, Amer. Geophys. Union, 21–48.

Wittenberg, A. T., 2002: ENSO response to altered climates. Ph.D. thesis, Princeton University, 475 pp.

——, A. Rosati, N.-C. Lau, and J. J. Ploshay, 2006: GFDL's CM2 global coupled climate models. Part III: Tropical Pacific climate and ENSO. *J. Climate,* **19,** 698–722.

Wu, R., 2002: Processes for the northeastward advance of the summer monsoon over the western North Pacific. *J. Meteor. Soc. Japan,* **80,** 67–83.

——, and B. Wang, 2000: Interannual variability of summer monsoon onset over the western North Pacific and the underlying processes. *J. Climate,* **13,** 2483–2501.

——, and ——, 2001: Multi-stage onset of the summer monsoon over the western North Pacific. *Climate Dyn.,* **17,** 277–289.

Xie, S.-P., K. Hu, J. Hafner, H. Tokinaga, Y. Du, G. Huang, and T. Sampe, 2009: Indian Ocean capacitor effect on Indo–western Pacific climate during the summer following El Niño. *J. Climate,* **22,** 730–747.

Yang, J., Q. Liu, S.-P. Xie, Z. Liu, and L. Wu, 2007: Impact of the Indian Ocean SST basin mode on the Asian summer monsoon. *Geophys. Res. Lett.,* **34,** L02708, doi:10.1029/2006GL028571.

Yu, L., and R. A. Weller, 2007: Objectively analyzed air–sea heat fluxes for the global ice-free oceans (1981–2005). *Bull. Amer. Meteor. Soc.,* **88,** 527–539.

Zhang, Y.-C., W. B. Rossow, A. A. Lacis, V. Oinas, and M. I. Mishchenko, 2004: Calculation of radiative fluxes from the surface to top of atmosphere based on ISCCP and other global data sets: Refinements of the radiative model and the input data. *J. Geophys. Res.,* **109,** D19105, doi:10.1029/2003JD004457.